Internal Report
DESY F41
HASYLAB 80/06
June 1980

The Extended X-Ray Absorption Fine Structure and its Applicability for Structural Analysis

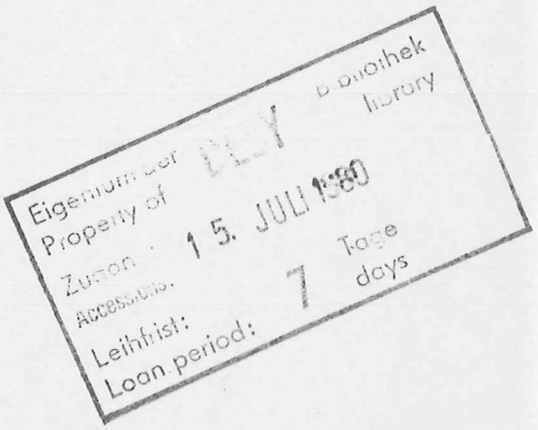

by

Peter Rabe

and

Ruprecht Haensel

The Extended X-Ray Absorption Fine Structure and its Applicability for Structural Analysis[+]

Peter Rabe and Ruprecht Haensel
Institut für Experimentalphysik, Universität Kiel,
Kiel, F.R. Germany

Abstract

The extended X-ray absorption fine structure (EXAFS) is observed above absorption edges of atoms in condensed matter. It is caused by the elastic scattering of the ejected photoelectrons by atoms surrounding the central absorbing atom. The periodicity of the EXAFS is determined by the interatomic distances and the scattering phases of the photoelectron wave. The amplitudes depend on the coordination number, the shape of the radial pair distribution and the electron-atom scattering probability. Hence this fine structure can be utilized to analyse the short range order around selected atoms. In this report we give a brief introduction to the theoretical background and compare experimental and calculated parameters which influence the shape of the EXAFS. Besides transmission experiments alternative techniques like reflectivity and electron or X-ray yield spectroscopy are discussed in view of the investigation of dilute samples. The analysis of the absorption fine structure is compared with competing diffraction techniques and the application of EXAFS is demonstrated on selected examples.

[+] abridged version of the Habilitationsschrift submitted to the Faculty of Mathematics and Natural Science of the University of Kiel by one of the authors (P.R.). A manuscript (in German) is available on request.

to be published in: Festkörperprobleme (Advances in Solid State Physics), Vol. xx, J. Treusch (ed.), Pergamon/Vieweg, Braunschweig (1980)

1. Introduction

The cross section σ_a of free atoms for the absorption of X-rays ($\hbar\omega > 1$ keV) is characterized by the absorption edges at energies, where the photons have sufficient energy to ionize the atom. Beyond the edges σ_a decreases monotonously (Fig.1). Structures in σ_a are observed only in the near edge region. The presence of other atoms in the neighbourhood of the absorbing atom, however, leads to an additional structure in the absorption coefficient μ, which extends up to several hundred electronvolts beyond the edge, the so called "extended X-ray absorption fine structure" (EXAFS).

For highly symmetric molecules with only one coordination sphere a single oscillation in μ is observed (Fig.2). In crystalline materials such as Cu (Fig.3) this fine structure is much more complicated. It represents a superposition of oscillations with different periodicities due to the different distances of coordination spheres as will be discussed later on. The remarkable properties of the EXAFS have been investigated since the thirties of this century [4]. The investigations demonstrated the direct relationship between the shape of the fine structure and the spatial geometry in the surroundings of the absorbing atom: The separation of minima and maxima of the EXAFS decreases with increasing distance between the central and the neighbouring atom. With increasing temperature i.e. with increasing thermal vibrations the EXAFS is strongly damped at high energies. In anisotropic crystals with lower than cubic symmetry the fine structure depends on the orientation of the polarization vector with respect to the crystal axes.

The generally accepted interpretation of EXAFS is a diffraction process of the photoelectron wave. The electrons excited by the absorption of photons are scattered at the neighbouring atoms. Outgoing electron wave ψ_o and its backscattered parts ψ_s superimpose and form the final state. The overlap of

the final state wave function with the ground state wave function and therefore the resulting magnitude of the transition matrix element depends on the relative phase of ψ_o and ψ_s and changes with photon energy, i.e. with the kinetic energy of the photoelectrons.

An increasing interest in the investigation of the EXAFS has been observed in the last years. One of the reasons for this are intensified efforts to calculate reliable values for scattering amplitudes and phases. Parallel to this the experimental conditions have been improved by the availability of high intensity X-ray sources as rotating anode generators and high energy electron accelerators. A breakthrough for the applications is the development of techniques to extract quantitative information about the local geometry around the absorbing atom from the EXAFS. Applying Fourier transform techniques to experimental spectra accuracies for bond lengths of better than 1% and for coordination numbers of better than 10% can be routinely obtained at present [5]. These values bear comparison with data derived from diffraction experiments on crystalline materials. Doubtless the classical scattering experiments still are superior to EXAFS experiments for materials with long range order. The former give information about the threedimensional electron density distributions, whereas EXAFS only yields a radial distribution function. In unoriented samples, however, the angular information in diffraction experiments is also lost and the remaining informations on the radial distribution functions require higher efforts for the extraction of the partial pair correlation functions. Furthermore, in diffraction experiments on highly dilute samples the interesting signal from the rare component in many cases is buried under the signal of the prevalent atomic species. In contrast only those partial correlation functions contribute to the EXAFS, which contain the absorbing atom.

A review is normally written, when a field has reached a certain stage of maturity. This review, however, appears at a time, when the extended X-ray absorption fine structure has just changed from an interesting phenomenon to a routine tool for structural investigations on unknown systems. Because of the limited size of this report, the emphasis necessarily is based of the authors' work in the last years. They apologize for the insufficient credit given to other workers.

2. Theoretical background and comparison with experiment

2.1. Single scattering picture

A schematic representation of the process which leads to EXAFS is shown in Fig.4. The lower part (a) shows the potentials of the central A and a neighbouring atom B with its K- and L-levels. By absorption of a photon the central atom is ionized and a photoelectron is created. The photoelectron wave leaves the atom A and is partially scattered at the atom B. The final state is a superposition of the outgoing and backscattered wave. The overlap between this wavefunction and that of the ground state determines the transition matrix element. By variation of the photon energy the wavelength of the electron wave is changed. In the energy range up to several hundred electronvolts above the absorption edge the free electron wavelength is of the same order as interatomic distances of nearest neighbours (Fig.4b). A variation of the photon energy changes the relative phases of outgoing and ingoing waves. This leads to a modulation in the matrix element and therefore the absorption coefficient oscillates around the average free atom value.

For the following discussion it is convenient to introduce the normalized expression

$$\chi(k) = (\mu - \mu_o)/\mu_o \qquad (1)$$

Here μ is the absorption coefficient, μ_o the monotonous part of μ and $k = 2\pi/\lambda$ the wavenumber of the photoelectron. For energies not too close to the edge k can be calculated from the free electron dispersion

$$k = \sqrt{\frac{2m}{\hbar^2}(\hbar\omega - E_o)} \qquad (2)$$

where $\hbar\omega$ is the photon energy and E_o the minimum of the free electron dispersion parabola .

Several approximations have been made to express $\chi(k)$ in a simple closed form [6-8]: i) The outgoing and the scattered waves are represented by plane waves at the site of the scatterer and the absorber respectively; ii) The asymptotic form for large momentum transfer is used, i.e. $k \cdot R \gg 1$ for all R (R being the distance between central atom and scatterer);iii) Only single scattering events are considered. With these approximations a single contribution $\chi_j^{l,l'}(k)$ to EXAFS which is caused by the scattering of an electron with angular momentum $\hbar l$ at an atom of the j-th coordination sphere to a state with angular momentum $\hbar l'$ can be expressed by

$$\Delta_j^{l,l'}(k) = k \cdot \chi_j^{l,l'}(k) = \int_0^\infty dR \, \frac{g_j(R)}{R^2} \, \mathrm{Im}\, \Lambda_j^{l,l'}(k,R) \cdot \exp(2ikR) \qquad (3)$$

$$\Lambda_j^{l,l'}(k,R) = f_j(\pi,k) \exp(-2R/\lambda + i\delta_l + i\delta_{l'}) \qquad (4)$$

Here $f_j(\pi,k)$ is the complex backscattering amplitude, the k-dependence of which is characteristic for the atomic number Z of the scatterer. The phases δ_l and $\delta_{l'}$, consider the influence of the absorber potential on the outgoing and scattered wave respectively. The distribution of the atoms around their average relative distance R_j is introduced by the pair correlation function $g_j(R)$ where

$$\int_0^\infty g_j(R)\, dR = N_j \qquad (5)$$

is the number of atoms in the coordination sphere j. The mean free path λ takes into account the damping of the electron wave by elastic and inelastic scattering processes and the finite lifetime of the core hole.

Using Eq.3 the EXAFS for oriented samples with lower than cubic symmetry at K- and L_I-edges, where transitions to only p-symmetric final states take place, can be written as

$$\chi(k) = -\sum_j 3\cos^2\theta_j \, \chi_j^{1,1}(k) \qquad (6)$$

The sum runs over all scattering atoms. θ_j is the angle between the X-ray polarization vector and the line between central atom and j-th scatterer. For unoriented samples the angular part averages out and the sum can be taken over all coordination spheres

$$\chi(k) = -\sum_j \chi_j^{1,1}(k) \qquad (7)$$

At L_{II}- and L_{III}-edges transitions to s- and d-symmetric final states are possible. In these cases the EXAFS takes the form

$$\chi(k) = \sum_j \left\{ \tfrac{1}{2}(1 + 3\cos^2\theta_j) \, |P_{21}|^2 \, \chi_j^{2,2} + \tfrac{1}{2} |P_{01}|^2 \, \chi_j^{0,0} + (1-3\cos^2\theta_j) \, P_{01}P_{21} \, \chi_j^{0,2} \right\} \cdot \left\{ |P_{21}|^2 + \tfrac{1}{2} |P_{01}|^2 \right\}^{-1/2} \qquad (8)$$

P_{01} and P_{21} are the radial dipole matrix elements between initial 2p state ($l = 1$) and the final states with angular momenta $l = 0$ and $l = 2$. For core transitions $|P_{21}| / |P_{01}| \cong 5$ [8], so that the second term in Eq.8 contributes only up to 2% to the total fine structure and therefore can be neglected in all practical cases. In isotropic samples the mixed term vanishes:

$$\chi(k) = \sum_j \left\{ |P_{21}|^2 \chi_j^{2,2} + \frac{1}{2} |P_{01}|^2 \chi_j^{0,0} \right\} \cdot \left\{ |P_{21}|^2 + \frac{1}{2} |P_{01}|^2 \right\}^{-1/2} \qquad (9)$$

Introducing the average distances R_j of the distribution $g_j(R)$, Eq.3 can be rewritten in the form

$$k \chi_j^{l,l'}(k) = |f_j(\pi,k)| \, |G_j(k)| \sin(2kR_j + \Phi_j^{l,l'} + \arg G_j(k)) \qquad (10)$$

with

$$\Phi_j^{l,l'}(k) = \delta_l(k) + \delta_{l'}(k) + \arg f_j(\pi,k) \qquad (11)$$

and

$$G_j(k) = \int_0^\infty \frac{g_j(R)}{R^2} e^{-2R/\lambda} e^{-ik(R - R_j)} d(R - R_j) \qquad (12)$$

In general a k-dependent term arg $G_j(k)$ occurs in the total phase. This means that the periodicity of the EXAFS is not only determined by the average distance R_j and the phase $\Phi_j^{l,l'}(k)$ which is independent on the geometrical structure, but also on the detailed shape of the pair distribution. As we shall see later, arg $G_j(k)$ in most cases can be neglected so that only the $\Phi_j^{l,l'}(k)$ have to be known to evaluate interatomic distances.

2.2. Scattering amplitudes and phases

Essential parameters for the evaluation of local geometries are the k-dependent complex scattering amplitudes $f(\pi,k)$ and the central atom phase shifts $\delta_l(k)$. The magnitude $|f(\pi,k)|$ of the scattering amplitude is directly correlated with the coordination numbers and the shape of the pair distribution. The k-dependence of the phases $\Phi(k)$ (Eq.11) together with the interatomic distance determines the periodicity of $\chi(k)$.

The shapes of $f(\pi,k)$ and $\delta_l(k)$ are characteristic for the atomic number of the elements. For high enough kinetic energies of the photoelectrons

($E_{kin} \gtrsim 50$ eV) only the core electrons are responsible for the scattering process. Changes of the electronic configuration as a result of different chemical environments only play a minor role. From this fact the concept of transferability of phase shifts and amplitudes has been developed [9, 10]. This means that $f(\pi,k)$ and $\delta_l(k)$ can be calculated individually for free atoms or $\Phi(k)$ and $|f(\pi,k)|$ can be extracted from EXAFS spectra of structurally known samples. These parameters can then be used for the investigation of structurally unknown systems.

Amplitudes and phases show a systematic variation with the atomic number Z. For several scattering atoms experimentally determined amplitudes A(k) representative for the variation from light (oxygen) to heavy (gold) elements are shown in Fig.5. The experimental amplitudes have been normalized to a coordination number N = 1 and to the distances R = 1 Å, i.e. Fig.5 represents the product $|f(\pi,k)| \cdot \exp(-2R/\lambda - 2\sigma^2 k^2)$ (mean square relative displacement σ^2: see section 2.5). The last term varies monotonously with k so that structures in A(k) are caused by $|f(\pi,k)|$.

At high kinetic energies the amplitudes decrease monotonously with k. Here the scattering amplitude can be described within Born's approximation. Using a screened Coulomb potential of the form

$$V(r) = - \frac{Ze^2}{r} e^{-r/a_s} \qquad (13)$$

with a_s the screening radius, the scattering amplitude is given by

$$f(\pi,k) = \frac{Z m e^2}{2\hbar^2 (k^2 + 1/4a_s)} \qquad (14)$$

For elements with medium Z a maximum in $|f(\pi,k)|$ shows up around 7-8 Å^{-1}. With increasing Z this maximum moves to higher k values and an additional minimum is observed at smaller k-values, e.g. in the case of I at k = 7 Å^{-1}.

For heavy elements like Au $|f(\pi,k)|$ oscillates over the whole k-range.

Calculated backscattering amplitudes $|f(\pi,k)|$ [8] fitted to the experimental data by a k-independent reduction factor of 0.6 - 0.7 (see section 2.4) and the mean square relative displacements σ^2 have been included in Fig.5b. The overall shape is in good agreement in all cases. At low k-values, however, the ratio of calculated and measured amplitudes is strongly k-dependent. Nevertheless, the position of peaks and valleys are well predicted by the theory.

The variation of the shape of $|f(\pi,k)|$ with atomic number Z can be used for the identification of the scattering atoms. The positions of minima and maxima in k-space are shown in Fig.6 as a function of Z. The open circles have been extracted from experimental EXAFS spectra [2]. The amplitudes have been corrected for the Debye-Waller-Factor with mean square displacements σ^2 calculated within the Debye-model [3]. The positions of peaks and valleys in calculated $|f(\pi,k)|$ [8] have been included in this figure (dots). Both theoretical and experimental values agree within the experimental uncertainty and the scatter of the calculated values. It is interesting to note that the linear regressions through the calculated points (straight lines) intersect the horizontal axis at Z = -8 (1st maximum), Z = 0 (1st minimum). Z = 21 (2nd maximum), Z = 39 (2nd minimum) and Z = 57 (3rd maximum). The last three values correspond to the beginning of the first and second row of transition elements and the lanthanides respectively.

The scattering phases $\Phi(k)$ determined experimentally represent the sum of the central atom phase shift δ_1 and the scatterer phase arg $f(\pi,k)$. For Cu and Au these $\Phi(k)$ determined from absorption spectra [11] are shown in Fig.7. For light elements (like Cu) these phases show a linear dependence on k. This means that the frequency of $\chi(k)$ is changed by the linear part of $\Phi(k)$ independent of the k-range under investigation. With increasing atomic number the phases $\Phi(k)$ deviate from the linear shape. The additional structures are directly related to the structures in $|f(\pi,k)|$.

The k-dependent parts of the experimental $\Phi_{exp}(k)$ are in fair agreement with the calculated values $\Phi_{theor}(k)$. Nevertheless, in some cases constant shifts between $\Phi_{exp}(k)$ and $\Phi_{theor}(k)$ are observed (see e.g. Cu in Fig.7). Part of these differences especially at low k-values can be compensated by an adequate choice of E_o (Eq.2) used for the conversion of the energy scale to the k-scale. However, the deviations at large k-values lead to uncertainties up to 0.03 Å for interatomic distances. Therefore, calculated phases should be used with care. At least they should be tested on materials with known geometry.

The systematic variation of $|f(\pi,k)|$ and $\Phi(k)$ is a direct consequence of the systematic variation of the phaseshifts η_l of the partial electron waves with angular momentum $\hbar l$ from which the scattering amplitude is calculated according to

$$f(\pi,k) = \frac{1}{k} \sum_{l=0} (-1)^l (2l+1) \cdot e^{-i\eta_l} \sin\eta_l \qquad (15)$$

Following Levinsons theorem [13] η approaches to $n_l\pi$ for k = o, where n_l is the number of bound states with quantum number l. For $k \to \infty$ the partial wave phase approaches to $\eta_l \to$ o. The peaks and valleys in $|f(\pi,k)|$ therefore can be attributed to the $\pi/2$ crossings of the η_l. These resonance like structures represent an analogon to the Ramsauer-Townsend effect [13], i.e. a sharp minimum in the cross section for elastic scattering of low energy electrons at free atoms. This minimum is attributed to the fact that the phase $\eta_o = n_o\pi$, while the η_l with $l \geqslant 1$ are too small to yield a significant contribution to the scattering amplitude.

2.3. Multiple scattering

Whereas for the bond lengths of nearest neighbours the single scattering events yield the only contributions to the EXAFS, multiple scattering is expected to contribute at larger distances. Calculated amplitudes for several paths of the photoelectrons in the fcc lattice of Cu are shown in Fig.8. Here we have adopted the notation (1-n-1) of Lee and Pendry [6]: The outgoing electron is scattering at an atom of the first shell, travels to a second atom of the first shell. The distance between the first and second scatterer corresponds to that between the central atom and the n-th shell. Apart from the case 1-4-1 all other paths only yield a weak contribution to the fine structure. The strong enhancement in the 1-4-1 multiple scattering contribution is due to the large amplitudes for forward scattering and the fact that the fourth shell atoms are shadowed by the first shell atoms in the fcc lattice. The Fourier transform F(r) of an EXAFS spectrum (see Section 3) of metallic Cu illustrates these additional multiple scattering contributions (Fig.9). Note that the fourth shell contributes to $\chi(k)$ with a signal comparable to that of the third shell, although the ratio of coordination numbers $N_4/N_3 = 1/2$. Furthermore, $\chi_4(k)$ should be reduced according to the factors $1/R^2$, $\exp(-2R/\lambda)$ and the larger Debye-Waller factor (see section 2.5).

From inspection of the peak positions in $|F(r)|$ and $\mathrm{Re}(F(r))$ it can be seen that the additional phase shift in $\chi_4(k)$ introduced by the multiple scattering amounts approximately to π : For the first three shells Re F(r) has a minimum where $|F(r)|$ has a maximum. In contrast Re F(r) of the fourth shell shows a sign reversal. Comparable values for the phaseshift introduced by forward scattering have been found in various cases, where a scattering atom is shadowed by another scatterer [14, 15]. All experiments seem to confirm, that the multiple scattering introduces only a weak additional k-dependence, i.e.

to a good approximation the frequency of the absorption fine structure remains unchanged.

2.4. Relaxation and multielectron processes

As discussed in section 2.2. the scattering amplitudes calculated within one-electron-theories successfully describe the shape of the experimentally determined EXAFS amplitudes. The absolute values of the amplitudes, however, differ by typically a factor of about 0.6 - 0.7. These differences, which severely impede the transferability of calculated scattering amplitudes are caused by relaxation processes in the central atom core after a single electron excitation. The scattering amplitudes are evaluated under the assumption, that the dominating process is a transition of a single electron to a continuum state leaving the ionized atom in its only partially relaxed ground state. Rehr et al. [16] have estimated the high energy limit of the reduction of the EXAFS amplitudes. They assume, that the ratio between experimental and calculated amplitudes is given by

$$S_o^2 = \left| \langle \Psi'_{Z-1} | \Psi_{Z-1} \rangle \right|^2 \qquad (16)$$

where Ψ'_{Z-1} and Ψ_{Z-1} are the Z-1 electron wave function of the relaxed and unrelaxed ion. Selfconsistent field calculations gave values of S_o^2 for halogen atoms and molecules as shown in Table 1. The value for Br_2 (0.64) is in good agreement with the value 0.62 used by Lee and Beni [17] to obtain a reasonable agreement between calculated and measured EXAFS amplitudes.

In all cases the molecules show smaller reduction factors than free atoms. This has been attributed to a further relaxation in the molecule, where the passive electrons not only can relax to the core, but where additionally a charge transfer to the neighbouring atom is possible.

A recent comparison of experimental and calculated backscattering amplitudes for liquid and gaseous Br_2 [18] yielded a reduction factor of 0.8 at high energies ($k > 8$ Å^{-1}) increasing to 1 below $k = 5$ Å^{-1}. This variation has been explained by a decrease in the overlap between Ψ'_{Z-1} and Ψ_{Z-1}. The escape of a photoelectron with low energy may be described in the adiabatic approximation, which predicts a complete overlap Ψ'_{Z-1} and Ψ_{Z-1}. At higher energies (sudden approximation) multiple excitations lead to an effective reduction of the overlap. The probability for multiple excitation increases with energy, reaching the maximum value several times the excitation energy, in qualitative agreement with the EXAFS results.

2.5. Pair distribution

2.5.1. Thermal disorder

At not too high temperatures the distribution of the atoms around their equilibrium position R_j can be described by a Gaussian distribution. Using a mean square relative displacement σ_j^2 between the central atom and the scatterers in the j-th coordination sphere and neglecting for the asymmetry introduced by $1/R^2$ and $\exp(-2R/\lambda)$ over this distribution, Eq.12 reduces to

$$G_j(k) = \frac{1}{R_j^2} \exp(-2k^2 \sigma_j^2) \cdot \exp(-2R_j/\lambda) \qquad (17)$$

Note that in this case $\arg(G_j(k)) = 0$, so that the periodicity of $\chi(k)$ in Eq.10 is only determined by the interatomic distance R_j and the structurally independent phase $\Phi_j^{l,l'}(k)$.

The simplest model to calculate the mean square relative displacements σ^2 as a function of temperature is the Einstein model:

$$\sigma_E^2 = \frac{\hbar}{2\mu\omega_E} \coth \frac{\hbar\omega_E}{2KT} \qquad (18)$$

with μ the reduced mass. In this model for a fixed Einstein frequency ω_E, σ^2 is independent of the distance between the central and scattering atom, i.e. a variation of the correlation of the atomic motion with R_j is not taken into account. Nevertheless, σ_E^2 yields reliable values over a wide range of temperatures for the first shell in lattices with a basis [19].

For nearest neighbours in lattices without a basis and for more distant shells a Debye-Model which explicitly takes into account the correlation of atomic motion is the more appropriate approximation [3]

$$\sigma_j^2 = 2\sigma_\infty^2(1 - \gamma_j) \qquad (19)$$

with

$$\sigma_\infty^2 = \frac{3\hbar}{2\mu\omega_D} \left\{ \frac{1}{4} + \left(\frac{T}{\Theta}\right)^2 \int_0^{\Theta/T} \frac{x}{e^x - 1}\, dx \right\} \qquad (20)$$

and

$$\gamma_j = \frac{3\hbar}{2\sigma_\infty^2 \mu\omega_D} \left\{ \frac{1 - \cos(q_D R_j)}{2(q_D R_j)^2} + \frac{T}{q_D R_j \Theta} \int_0^{\Theta/T} \frac{\sin(q_D R_j \frac{T}{\Theta} x)}{e^x - 1}\, dx \right\} \qquad (21)$$

where ω_D, Θ and q_D are the Debye frequency, temperature and wavenumber respectively. σ_∞^2 describes the individual motion of the atoms and $\gamma_j \sigma_\infty^2$ the in phase motion, which does not influence the EXAFS amplitudes. The displacement correlation function γ calculated within this model is shown in Fig.10. As expected the correlation reduces with decreasing temperature, but even at $T = 0$ it amounts to 10-15 % of the total motion for nearest neighbours. The oscillations which are observed in γ as function of $q_D R$ are caused by the weighting of the Brillouin zone boundary. A similar effect is also expected when more realistic density of states data are used.

Experimental σ^2 from EXAFS measurements of metals and binary compounds have been compared with values calculated within the Debye approximation [3].

As shown in Fig.11 the calculated and measured values agree within the experimental uncertainties. At higher temperatures the pair distribution may significantly deviate from a symmetric distribution [20]. The consequences of a general pair distribution on the amplitudes and phases of EXAFS are outlined in the next section.

2.5.2. Structural disorder

The simplest case of structural disorder are two close lying shells, which cannot be resolved e.g. by Fourier transform techniques described in section 3. The superposition of two contributions (Eq.10) to $\chi(k)$ leads to a beating in k-space. For the general case of two different pair distributions $(g_1(r) \neq g_2(r))$ i.e. $G_1(k) \neq G_2(k)$ with different scattering atoms ($f_1 \neq f_2$ and $\Phi_1 \neq \Phi_2$) at equilibrium positions R_1 and R_2 the sum of the two contributions can be expressed by

$$\chi(k) = \chi_1(k) + \chi_2(k) = \frac{1}{k}|f||G| \cdot \sin(2kR + \Phi + \arg G) \qquad (22)$$

with

$$|f||G| = |f_1||G_1| \left\{ 1+c^2+2c\cos(2\Delta Rk+\Delta\Phi+\Delta\arg G)\right\}^{1/2} \qquad (23)$$

$$\arg G = \tan^{-1} \frac{\sin(\Delta Rk + \frac{\Delta\Phi}{2} + \arg G_1) - c\sin(\Delta Rk + \frac{\Delta\Phi}{2} + \arg G_2)}{\cos(\Delta Rk + \frac{\Delta\Phi}{2} + \arg G_1) + c\cos(\Delta Rk + \frac{\Delta\Phi}{2} + \arg G_2)} \qquad (24)$$

$$\left.\begin{aligned} &R = (R_1+R_2)/2 \quad \Delta R = R_1-R_2 \quad \Phi = (\Phi_1+\Phi_2)/2 \quad \Delta\Phi = \Phi_1-\Phi_2 \\ &\Delta\arg G = \arg G_1 - \arg G_2 \\ &c = |f_2||G_2| \,/\, |f_1||G_2| \end{aligned}\right\} \qquad (25)$$

Assuming small Gaussian distributions leads to $\Delta\arg G = 0$. For identical atoms in the two shells we obtain $\Delta\Phi = 0$, so that the differences in interatomic distances can directly be calculated from the beating nodes in the amplitudes. The shape of amplitude and phase of a two shell model EXAFS for various constant parameters c and $\Delta R = 0.3$ Å is shown in Fig.12. Whereas the differences of distances can only be extracted directly from the Fourier transform F(r) with a considerable uncertainty, ΔR can be determined from the position of minima in $|f| \cdot |G|$ and the inflection points in arg G via $\Delta R = \pi/2k$ with an accuracy better than 0.01 Å.

A more general case is a continuous asymmetric pair distribution. For an analytic expression

$$g(R) = \begin{cases} \frac{1}{a} \cdot R^2 \cdot \exp \frac{R_o - R}{a} & \text{for } R \geq R_o \\ 0 & \text{elsewhere} \end{cases} \qquad (26)$$

which can be used as a first approximation to describe the distribution of nearest neighbours in a dense random packing of hard spheres, G(k) and $\Delta R = (2k)^{-1} \arg G(k)$ are shown in Fig.13. With increasing asymmetry, i.e. increasing parameter (a) the phase contribution increases, especially at lower k-values. Weighting the fine structure in different k-ranges would pretend different average interatomic distances, if the additional structure dependent phase term arg G(k) (Eq.10) is neglected. These differences have to be kept in mind when comparing results from alternative techniques for structural analysis. In X-ray diffraction experiments e.g. the signal dominates at low k-values where the EXAFS cannot be interpreted in the simple way of Eq.10. This will be discussed in detail in section 5.

2.6. Anisotropy

According to Eq.s 6 and 8 the EXAFS of materials with lower than cubic symmetry depends on the orientation of the polarization vector $\vec{\varepsilon}$ with respect to the line between central and scattering atom. This angular dependence can be

used to determine the three-dimensional arrangement of atoms in a sample.

Anisotropic EXAFS experiments using polarized synchrotron radiation have been reported on a single crystal of Zn [23], on a layered 2H-WSe_2 crystal [24], on oriented Br_2 molecules adsorbed on graphite [25] and on a layered GeS crystal [26]. We briefly describe the results for GeS.

GeS has an orthorhombic unit cell. It easily cleaves in the ac-plane. With a polarization vector in this plane an angular dependence of the EXAFS is expected when the crystal is rotated around the b-axis (Fig.14). In this arrangement the anisotropy can be studied without changing the effective thickness of the sample, so that no distortions of the spectra are expected.

The EXAFS spectra at the Ge K-edge for $\vec{\varepsilon} \parallel \vec{a}$ and $\vec{\varepsilon} \parallel \vec{c}$ (Fig.15, upper part) show significant differences over the whole k range. A quantitative analysis of these spectra is possible in real space as discussed in detail in section 3. The magnitude of the Fourier transform of the EXAFS are compared in Fig.15 (lower part) with crystal structure data derived from X-ray diffraction experiments.

Using interatomic distances R_j, the angles α_j and γ_j (Fig.14) and the coordination numbers N_j the contributions to $|F(r)|$ due to S- and Ge-scatterers have been calculated. They have been introduced in Fig.15 as vertical bars (S solid, Ge dotted). The positions of the bars give the expected positions of peaks in $|F(r)|$, the lengths represent the amplitudes of structures in $|F(r)|$. Note that according to the k-dependent parts of the phases $\Phi(k)$ the peaks in $|F(r)|$ are shifted to smaller interatomic distances. The result shows that in the range $0 < r < 5$ Å between seven ($\varepsilon \parallel c$) and eleven ($\varepsilon \parallel a$) scattering shells contribute to EXAFS, which are not completely resolved. Nevertheless, the average of the several group of bars shows an excellent agreement with structures in $|F(r)|$ for both cases.

3. Evaluation of structural parameters

The initial step of data analysis is the removal of the monotonous background absorption due to weaker bound electrons. The shape of the absorption coefficient below the edge can be described by

$$\mu_b = C\,(\hbar\omega)^{-3} + D\,(\hbar\omega)^{-4} \qquad (27)$$

Fitting this equation to the experimental data below the edge and extrapolating μ_b beyond the edge yields the total absorption coefficient of the inner shell under investigation: $\mu = \mu_o(1 + \chi)$ (see Eq.1). The second step is the conversion of the energy scale to the k scale. The choice of E_o (Eq.2) is somewhat arbitrary (see below). In most cases the position of the absorption edge is used to fix E_o. The third step is the removal of the atomic background μ_o. Experience shows that with a polynomial of second or third degree in k the contribution of μ_o can be fitted. The remaining background can be eliminated by Fourier filtering [10].

To evaluate structural parameters the EXAFS can be fitted with parametrized amplitudes $|f(\pi,k)|$ and phases $\Phi(k)$. The advantage of this procedure is that the experimental data can be analyzed without further treatment. Boundary effects which lead to an effectively reduced range of the data do not occur as in the Fourier transform technique. Because of the rapidly increasing number of parameters with an increasing number of contributions to $\chi(k)$, a fitting procedure is only applicable to simple EXAFS spectra or only in connection with techniques discussed below.

The most widely applicable procedure to separate contributions with different frequencies (distances) is the Fourier transform [10, 27-29]. Taking the transform of $k^n \Delta(k)$ (Eq.3) with respect to exp(2ikr) we obtain a complex radial structure function according to

$$F(r) = \frac{1}{\sqrt{2\pi}} \sum_j \sum_{l,l'} B_j \int_0^\infty d(2k)\, \exp(2ikr)\, k^n \Delta_j^{l,l'}\, W(k)$$

$$= \sum_j \sum_{l,l'} B_j \int_0^\infty dR\, \frac{g_j(R)}{R^2} \frac{1}{2i} \left\{ \xi^{(n)}_{jll'}(r + R, R) - \xi^{*(n)}_{jll'}(-r + R, R) \right\} \quad (28)$$

with

$$\xi^{(n)}_{j,l,l'}(r+R, R) = \frac{1}{\sqrt{2\pi}} \int_{-\infty}^{\infty} dr'\, \frac{w^{(n)}(r+R-r')}{(2i)^n}\, \lambda_j^{l,l'}(r',R) \quad (29)$$

and

$$\lambda_j^{l,l'}(r',R) = \frac{1}{\sqrt{2\pi}} \int_0^\infty d(2k)\, \Lambda_j^{l,l'}(k,R)\, \exp(2ikr') \quad (30)$$

Here $w^{(n)}$ is the n-th derivative of the Fourier transform of the effective window function W(k) formed by the limited k-range where EXAFS can be observed and a window used to smooth the boundaries, i.e. to reduce side lobes in the Fourier transform. The Fourier transform F(r) is a convolution of the pair distribution function $g_j(R)$ (modified by the factor $1/R_j^2$) and the peak function $\xi^{(n)}$. The B_j account for the angular dependent parts and the dipole matrix elements in Eq.s 6, 8 and 9. Structures in real space are determined by $\xi_j^{(n)}$ in the positive and $\xi_j^{*(n)}$ in the negative half space. The positions of maxima in $|F(r)|$ are shifted to smaller values compared to the real interatomic distances. This is caused by the k-dependence phase shifts $\Phi(k)$ introduced by the scattering process. This shift amounts to typically 0.2 to 0.4 Å.

Single contributions to $\chi(k)$ can be isolated by an inverse Fourier transform. Using an appropriate window function W(k) (Eq.28) the information about a single scattering shell is contained in a limited range in real space. The

EXAFS caused by a single shell can then be calculated from

$$\bar{\Delta}_j(k) = \sqrt{2\pi} \int_{r_1}^{r_2} dr\, F(r)\, \exp(-2ikr)/(k^n\, W(k)) \quad (31)$$

Eq.31 is the starting point for the determination of local geometrical parameters of a single scattering shell and the scattering amplitudes and phases. From the total phase of $\bar{\Delta}_j(k)$ the scattering phases $\Phi_j(k)$ (with known interatomic distances) or the R_j (with known phases $\Phi_j(k)$) can be determined. The magnitude $|\bar{\Delta}_j(k)|$ yields the amplitude of a single shell, from which the backscattering amplitude, coordination numbers and Debye-Waller factors can be evaluated.

All k dependent parameters evaluated in this way are only uniquely defined if the zero of the energy scale E_o for the conversion to the wavenumber scale k is known. For materials which show a free electron dispersion like Al, E_o is given to a good approximation by the bottom of the conduction band. In general, however, E_o is unknown and therefore has to be included in the structural analysis. Changing the zero of energy by ΔE_o the wavenumber scale k changes to a new scale

$$k' = \left(k^2 - \frac{2m}{\hbar^2} \Delta E_o\right)^{1/2} \quad (32)$$

which leads to a phase

$$\Phi'(k') = \Phi(k) + \frac{2mR\Delta E_o}{\hbar^2 k} \quad (33)$$

An incorrect E_o modifies the phase, especially at small k-values. It should be noted that a variation of E_o cannot produce an arbitrary interatomic distance. In contrast to E_o a variation ΔR of the interatomic distance leads to an additional phase term $\Delta\Phi = 2k\Delta R$. Several techniques have been used to reduce the influence of E_o:

i) A multiplication of the fine structure with k^n weights the EXAFS at large k-values.

ii) The E_o is used as a free parameter [10]. The interatomic distances e.g. are determined from

$$R_j(k) = (\arg \overline{\Delta}_j(k) - \Phi_j(k))/2k \qquad (34)$$

A deviation of $R_j(k)$ from a constant value can be eliminated with a variation of E_o. The R(k) = const determined in this way yields the correct interatomic distance with a high reliability.

4. Experimental techniques

4.1. Light sources and monochromators

A typical experimental setup for transmission experiments in the X-ray range is shown in Fig.16 [30]. Here the Deutsches Elektronen-Synchrotron DESY serves as light source. The monochromator consists of a single axis goniometer and a channel cut Ge- or Si-crystal. The monochromatic radiation is monitored by ionization chambers. The signals of the chambers are amplified by fast current amplifiers and converted to pulse trains, the frequencies of which are proportional to the output voltages of the amplifiers. The number of pulses of the signal channel integrated within a preset number of counts of the reference channel are stored in a computer. The computer controls the angular setting of the goniometer and the position of the table onto which ionization chambers and samples are mounted.

Until some few years back only the continuous bremsstrahlung of conventional X-ray tubes has been used for these experiments. The synchrotron radiation of electron accelerators in the GeV range has provided new intensive sources which have stimulated the development of X-ray spectroscopy [31].

A schematic comparison of synchrotron radiation and the bremsstrahlung is shown in Fig.17. The bremsstrahlung is emitted isotropically from the anode whereas the synchrotron radiation is confined to a small vertical cone of typically 0.1 mrad at 10 keV photon energy. The spectral distribution of X-ray tubes is the superposition of the continuous bremsstrahlung and the characteristic lines which severely limits the useful spectral range. The advantage of the synchrotron radiation is its structureless spectrum. X-ray tubes normally have a high constancy in time. In contrast an electron accelerator is a pulsed light source with a pulse separation between 2ns and 1 µs and pulse lengths of 0.1 to 1ns depending on the mode of operation [31]. An additional variation of the intensity at synchrotrons is due to the acceleration cycle e.g. with a frequency at DESY of 50 cps. The time structure may make high demands on the time resolution and linearity of detectors.

The synchrotron radiation is linearily polarized in the plane of the electron orbit. Above and below this plane an additional vertically polarized component comes up. The degree of polarization depends on the angular range of radiation used in the experiment. It amounts to more than 80% for typical exit slits of several millimeters height. For X-ray tubes the degree of polarization is difficult to calculate. It depends on the wavelength, the take-off angle from the anode, the anode material and the acceleration potential.

A quantitative comparison of intensities of an X-ray tube (Cu-anode, 45 keV, 500 mA) and the synchrotron radiation of DESY is shown in Fig.18. Clearly the brightness of the synchrotron radiation surmounts that of the bremsstrahlung by orders of magnitude. At storage rings the intensity can even be increased by at least one order of magnitude by increasing the electron current and inserting bending magnets with higher magnetic fields (wigglers).

The decisive magnitude is the number of photons available at the experiment. Using flat crystals and conventional X-ray sources count rates of the order

of 10^4 s^{-1} are available. The fluxes can be increased to 10^6 - 10^7 s^{-1} using focusing crystal optics and rotating anode generators making feasible the study of dilute samples down to concentrations of e.g. 1% Fe in H_2O [32, 33]. At storage rings photon fluxes up to 10^{12} s^{-1} have been reported [34], so that even monolayers of atoms on bulk substrates can be studied.

4.2. Detection schemes

4.2.1. Primary processes: Transmission and Reflectivity

The simplest arrangement to determine the absorption coefficient is a transmission experiment. The parameter which determines for a given primary intensity I_o the signal to noise ratio is the thickness d of the sample. Several criteria have been used to optimize d (noise of primary (I_o) and transmitted (I) intensity, background) [35, 36]. In all cases the suitable values for μd lie between 1.3 and 2.5. If the noise is mainly given by the noise of I, as it is usually the case at high intensity X-ray sources, the optimal thickness is given by

$$d = \frac{2}{\mu} \qquad (35)$$

For $\mu = \mu_b + \mu_s$, where μ_b is a background absorption and μ_s the inner shell absorption under investigation the statistical relative uncertainty amounts to

$$\frac{\Delta\mu_s}{\mu_s} = \frac{e}{2} \cdot \frac{\mu}{\mu_s} \cdot \frac{1}{\sqrt{I_o}} \quad ; \qquad e = 2.718 \ldots\ldots \qquad (36)$$

Another important quantity for transmission experiments is the homogeneity of the sample thickness. The ratio of measured (χ_m) and true (χ) EXAFS amplitudes can easily be calculated for a sample where the fraction R of the total area consists of holes while the rest has a homogeneous thickness (Fig.19). As expected small inhomogeneitiesin thick samples lead to a significant reduction of EXAFS amplitudes. For the evaluation of structural parameters from the amplitudes of EXAFS (coordination numbers, Debye-Waller factor) special care has to be taken for the sample preparation.

The reflectivity of a sample is determined by the complex index of refraction $n = 1 - \delta - i\beta$. Below the critical angle of total reflection φ_c the energy dependence of the reflectivity is mainly determined by the imaginary part β, i.e. the absorption coefficient [37, 38] (Fig.20). The possible applications of reflectivity experiments results from the sensitivity to superficial regions. The penetration depth z of X-rays ($I = I_o/e$) is given by

$$z = \frac{hc}{\pi\sqrt{8}} \cdot \frac{1}{\varphi_c(\hbar\omega)} \cdot \left\{ \sqrt{(x^2 - 1)^2 + y^2} - (x^2 - 1) \right\}^{-1/2} \qquad (37)$$

where $x = \varphi / \varphi_c$ and $y = \beta/\delta$. For glancing angles φ below φ_c the penetration depth is typically of the order of 20 - 50 Å (Fig.21). z increases rapidly above φ_c.

In principle the investigation of the reflectivity offers the possibility to study depth profiles, i.e. geometrical structures in different depths of a sample. Compared to the techniques discussed below, which measure the absorption-coefficient via secondary processes,the total reflection as a primary process has the advantage of high intensities. An obvious obstacle of the reflectance method is the exacting sample preparation. Because the reflectivity has to be measured at extremely small glancing angles high demands are made to surface roughness and flatness.

4.2.2. Secondary processes: X-ray fluorescence, electron emission

The detection of products which are generated by secondary processes after the excitation of the central atom are alternative techniques to measure the absorption coefficient. The goal of these techniques is the study of dilute

samples. This is equivalent to a reduction of the ranges in real space from which informations are obtained. Samples to be investigated with these techniques can be grouped in two categories: i) Thick samples with a low concentration of guest atoms. Typical examples are organometallic compounds (e.g. biomolecules) and dilute alloys. A reduction of the information range in this case means the suppression of signals which are caused by absorption at matrix atoms; ii) Thin but concentrated samples: Examples which fall into this category are thin films, surfaces and adsorbates on solids.

Following the absorption process the central atom relaxes under emission of X-ray fluorescence photons or Auger electrons. In molecules or crystals the energy of the excited state can be transferred to the matrix. The radiative decay of intermediate states (excitons) gives evidence of the existence of the primarily excited states. The yield of all these secondary byproducts carry the information about the transition probability.

The energy of fluorescence photons is characteristic for the atomic number. A selective detection of these photons suppresses the background which is caused by the absorption at weaker bound electrons. This technique is competing with simple absorption experiments on highly dilute samples. The statistical relative uncertainty in a fluorescence experiment on thin concentrated samples of thickness d is given by

$$\frac{\Delta\mu_s}{\mu_s} = \left\{ I_o \varepsilon \frac{\Omega}{4\pi} \mu_s d \right\}^{-1/2} \qquad (38)$$

and on thick dilute samples by

$$\frac{\Delta\mu_s}{\mu_s} = \left\{ \frac{\mu(E) + \mu(E_F)}{I_o \varepsilon \frac{\Omega}{4\pi} \mu_s(E)} \right\}^{1/2} \qquad (39)$$

Here E und E_F are the energy of the exciting and the fluorescence photons respectively, ε the fluorescence yield and Ω the effective solid angle. A comparison with Eq.36 shows that $\Delta\mu_s / \mu_s \sim \mu_s^{-1}$ in transmission while $\Delta\mu_s / \mu_s \sim \mu^{-1/2}$ in the yield experiment, i.e. at low concentration the secondary yield technique does better concerning the signal to noise ratio.

The electrons leaving the sample can be classified into direct photoelectrons, Auger electrons and inelastically scattered electrons. The yield of unscattered photoelectrons reproduces the absorption coefficient only if these electrons are collected over a solid angle of 4π because their angular distribution varies with photon energy [39]. In general this demand is not fulfilled at solid surfaces. Therefore structural analyses by means of electron yield techniques have only been performed by monitoring the unscattered Auger electrons or the yield (partial or total) of inelastically scattered electrons.

In the Auger electron yield technique [40] the energy of the electrons is characteristic for the absorbing atom so that the signal from the substrate is suppressed in the same way as in the fluorescence technique. The mean free path of low energy electrons amounts to only several Angstroms, so that the Auger electrons carry informations from only a few atomic layers at the surface. The main problem of this technique is the low yield. Besides the adverse ratio of penetration depth of photons and escape depth of the electrons the useful solid angle for the monochromatization and detection of the electrons limits the number of collected electrons. Additional problems arise in the soft X-ray region. Here the energy of the Auger electrons may coincide with the energy of unscattered photoelectrons producing artificial structures in the yield spectra [41].

The simplest experiment is the detection of the total electron yield. All electrons are collected as a function of photon energy. Several experiments

have shown the equivalence of absorption and total yield spectra [42, 43] as demonstrated for Ni in Fig.22. The angular dependence of the direct photoelectrons which leads to the nonequivalence of photoelectron yield and absorption coefficient averages out for the following reasons: i) In polycrystalline materials the arbitrary arrangement of microcrystallites relative to the polarization vector leads to an effective averaging over all solid angles.
ii) Not too far from the edges the total yield mainly contains secondary electrons produced by the cascade of Auger electrons. This is confirmed by the fact that absorption and emission show an excellent agreement of structures in the near edge region and that no shifts of the edges according to the work-function of the sample are observed. Compared to the absorption coefficient the total yield drops off weaker at higher energies which qualitatively can be traced back to the increasing contributions of photoelectrons. The EXAFS, however, has been shown to be identical in both cases. iii) The depth in the sample from which informations are carried to the surface is large compared to the mean free path of single electrons. This is not only due to multiple inelastic scattering but also to reabsorption of fluorescence photons in superficial regions. Yield measurements as a function of the photon glancing angle [42] and yield spectra of thin films on substrates [43] have shown that the information range in the sample amounts to typically 1000 to 2000 Å.

The essential parameter for total yield experiments is the photon glancing angle. For small glancing angles the penetration of the photons decreases i.e. the yield increases (Fig.23). The yield from a thin layer of thickness d is given by

$$Y = \frac{I_o}{2}(1-R)\cdot\frac{\mu}{\sin\varphi'}\cdot\frac{1-\exp(-d(\mu'/\sin\vartheta + \mu/\sin\varphi'))}{\mu'/\sin\vartheta + \mu/\sin\varphi'}\cdot\frac{\Omega}{4\pi} \qquad (40)$$

where $1/\mu$ and $1/\mu'$ are the extinction lengths of the primary and secondary

radiation and φ' and ϑ the angles between these beams in the sample and the surface respectively; Ω is the solid angle where the secondaries can be detected, R the reflectivity and I_o the primary intensity. For $\sin\varphi' \ll \mu$ the yield practically is independent of the absorption coefficient. The choice of the optimal glancing angle is a compromise between an enhancement of the signal and the fading of structures at small glancing angles.

5. Comparison of EXAFS with diffraction techniques

The classical techniques for structural investigations are diffraction of X-rays, neutrons or electrons. In ordered systems the accuracies for atomic positions achievable with these experiments are far superior to the data obtainable from the EXAFS at present. In disordered systems, however, the angular information is also lost in diffraction experiments so that as in EXAFS only the information about the radial distribution remains.

In scattering experiments the intensity of elastically scattered photons, neutrons or electrons is measured as a function of momentum transfer $Q = 4\pi\sin\Theta/\lambda$ (equivalent to 2k in EXAFS spectra). The analysis of these data in general necessitates extensive corrections concerning intensity losses due to absorption, incoherent scattering and polarization. For EXAFS the electron source and the detector are located at the site of the absorbing atom. According to this local character these type of corrections are not necessary in the analysis of EXAFS.

Analogous to Eq.28 the radial distribution function derived from a Fourier transform of the diffraction pattern can be expressed as

$$F(r) = \sum_i c_i \sum_j \int_0^\infty dR\, \frac{g_{ij}(R)}{R^2}\,\frac{1}{2i}\left\{\xi_{ij}^{(n)}(r+R, R) - \xi_{ij}^{*(n)}(-r+R, R)\right\} \qquad (41)$$

Here the peak function ξ_{ij} is the Fourier transform of the product of the individual scattering factors and the window function and g_{ij} the pair distribution discussed in section 2.5. For photon energies not too close to absorption edges the peak function can be calculated from known quantities in contrast to EXAFS.

The main differences to the complex structure function F(r) which can be evaluated from EXAFS spectra is the additional sum over the scattering atoms i which are present in the sample with a concentration c_i. The radial structure function calculated from the diffraction pattern is a superposition of all pair correlations. Whereas in elemental materials the analysis of a diffraction pattern can be performed with the same ease as EXAFS spectra this fact leads to significant complications in multicomponent systems. For a sample containing N different atomic species, Eq.41 is a superposition of N(N+1)/2 individual pair correlation functions which practically cannot be resolved in materials with large N.

An essential advantage for EXAFS is the fact that the central atom is defined by the absorption edge reducing the number of superimposed pair correlations to N. Furthermore, the shape of the backscattering amplitudes $f(\pi,k)$ gives additional information about the type of the scattering atom so that even these N pair correlations can be resolved in favoured cases.

To get informations comparable to that from EXAFS several independent scattering experiments with different weighting of the scattering probabilities of the atomic species are neccessary, e.g. combination of X-ray scattering (normal or anomalous dispersion), magnetic and nuclear neutron scattering, neutron scattering on materials with isotopic and isomorphous substitution of scattering atoms. A detailed discussion of these experiments is beyond the scope of this paper. The reader is referred to the literature on this subject [45].

A special technique utilizing the anomalous dispersion of X-rays has been proposed by Shevchik[46, 47]: The photon energy is modulated in a range close to an absorption edge. Only those scattered photons are filtered out, the intensity of which varies with photon energy. This yields a diffraction pattern caused by only those pair correlations which contain at least one atom showing the anomalous dispersion. Compared to EXAFS the disadvantage seems to be the higher experimental effort. Though the applicability has not yet been proved experimentally it seems questionable whether the same sensitivities can be achieved especially for highly dilute samples. Principally this experiment supplies no more information than static experiments at two different wavelengths and subsequent numerical evaluation of the difference spectrum.

An important difference between an X-ray diffraction pattern and EXAFS is the respective region of momentum transfer. In the scattering experiment typically a range of $0<Q<12$ Å^{-1} at a wavelength of 1 Å is accessible. Compared with this EXAFS is observed in a typical range of 6 Å$^{-1}< 2k < 25$ Å^{-1} (Fig.24). The range below $k \approx 3$ Å^{-1} in general cannot be interpreted in terms of the simple single scattering picture as outlined in section 2.1. The loss of information in the low k-range leads to an increased sensitivity to variations of interatomic distances. With increasing disorder structures in the absorption coefficient are damped at high k-values. Then the essential signal is hidden in ranges of k-space which are unaccessible to an easy interpretation. In amorphous systems where the disorder increases strongly with radial distance from the absorbing atom this high sensitivity has the consequence that practically only contributions from nearest neighbours are observed in the EXAFS beyond $k \approx 3$ Å^{-1} [22, 49].

For systems with symmetric pair distributions $g_j(R)$ comparable values for the average distance R_j and the numbers N_j of atoms in a coordination sphere are

derived from scattering and EXAFS experiments. On the other hand the additional k dependent phase term arg $G_j(k)$ in Eq.10 caused by a nonsymmetric pair distribution leads to different frequencies of the fine structure in different k ranges. An analysis of EXAFS spectra of such materials with a formalism derived for symmetric g(R) (Eq.17) pretends different R_j and N_j values compared to the X-ray scattering results according to the different weighting of the k and Q space. For those systems the detailed shape of the pair distribution has to be included in the evaluation of the local geometry which means a severe impediment to the general applicability of EXAFS.

6. Applications

The applicability of EXAFS for structural analysis has been demonstrated in a number of different fields in the last years. Within the limited frame of this report proper account cannot be given to all of them. The interested reader is referred to recent reviews, which cover the investigations of organometallic compounds [50-53], amorphous solids [22, 54, 55] , catalysts [56] and ionic conductors [57]. We rather present some few examples worked at by the own research group, which demonstrate the wide variety of possible applications in physics and chemistry.

6.1. Mean square relative displacements of atoms in a-Ge and c-Ge [49] .

As discussed in section 2.5.1. the thermal motion of nearest neighbours is correlated. For crystalline metals this correlation can be adequately described by a Debye model (Eqs19-21) which considers the in phase motion of the atoms. To test the range of validity of this model the temperature dependence of the mean square relative displacements of nearest and next nearest neighbours have been extracted from EXAFS spectra of crystalline Ge (c-Ge) and amorphous

Ge (a-Ge) above the K-edge.

Using Fourier transform techniques the contributions of the different shells to $\chi(k)$ have been extracted. A comparison of the total phases ($\arg \overline{A}_j(k)$, Eq.31) of a-Ge and c-Ge yields a difference in the nearest neighbours distance $\Delta R_{ac} = R_a - R_c = 0.003\ \text{Å} \pm 0.003\ \text{Å}$ at 80 K in agreement with the previous EXAFS results [58] . Data from X-ray diffraction measurements resulted in $\Delta R_{ac} = 0.07\ \text{Å}$ [59] . The nearest neighbour distance in a-Ge and c-Ge changes by less than 0.005 Å in the temperature range between 80 K and 300 K. This is consistent with the value of 0.0023 Å, which can be deduced from the thermal expansion coefficient of bulk c-Ge. Changes of σ_j^2 are compiled in Table 2. Using calculated backscattering amplitudes the absolute σ^2 for c-Ge at 80 K has been determined to be 0.0019 ± 0.0003 Å. The combination of these results is shown in Fig.25.

The thermal disorder of the first two shells in c-Ge shows significant differences. For the first shell only small changes of σ_1^2 are observed over the whole temperature range. This behaviour demonstrates the strong correlation of the atomic motions. For the second scattering shell a much stronger increase of σ_2^2 with temperature is observed. This enhancement is mainly introduced by a dynamical distortion of the tetrahedrous bond angle. At low temperatures σ_2^2 approaches σ_1^2, which means that the displacement correlation function γ (Eq.21) approaches a similar value for both shells. In a-Ge larger values of σ_1^2 with respect to c-Ge have been found over the whole temperature range. These differences of σ_1^2 at least give an estimate of the contribution of the static mean square relative displacement σ_s^2 to the total disorder in a-Ge. An extrapolation of σ_1^2 for a-Ge and c-Ge to T = 0 yields $(\sigma_s^2)^{1/2} = 0.05\text{Å} \pm 0.01$ Å. This value is significantly larger than the result of Polk [60], who calculated a value of 0.03 Å.

From the fact that no contribution from the second nearest neighbours is observable in the EXAFS of a-Ge a distortion of the tetrahedron angle of at least 10° has been estimated. This value is in agreement with values calculated in the continuous network model [60] and with X-ray scattering data [61]. In both cases a distortion of 10° is reported.

Values for σ^2 calculated within the Debye approximation have been included in Fig.25. Compared to the experimental values of both the nearest and next-nearest neighbours in c-Ge the theory predicts larger σ^2 and stronger increase with temperature in c-Ge i.e. the correlation is underestimated by this model in the case of covalent bonds.

6.2. Amorphous Metallic Alloys [22].

The EXAFS spectrum of $Fe_{80}B_{20}$ at the Fe K-edge is shown in Fig.26a. The Fourier transform (Fig.26b) is dominated by a maximum at 2 Å, which is a superposition of contributions from the nearest Fe- and B-neighbours. All higher coordination shells are substantially suppressed due to higher disorder.

Isolation of the contributions contained in the first maximum by an inverse Fourier transform of $|F(r)|$ in the range of 0.8 to 2.75 Å back into k-space allowed a separation of the partial Fe- and B-contributions with a two shell fit (see Fig.27). The results using a Gaussian pair distribution (arg G(k) = 0) and experimental phase shifts and scattering amplitudes of Fe are compiled in Table 3 (R_E, N_E and σ_E^2). A comparison with corresponding X-ray diffraction data [48] (R_D and N_D in Table 3) showsdeviations in R and even more dramatic in N. This disagreement is due to the fact that an inappropriate Gaussian pair distribution has been used to analyze the data. Approximating the pair distribution of $Fe_{80}B_{20}$ by a simple exponential (Eq.26 with a = 0.17 Å), which is consistent with a DRP (dense random packing of hard spheres) model [62] distribution function the data of R_E and N_E have been corrected according to the phase

term arg G(k) (Eq.10). These values (R_E^C, N_E^C in Table 3) are much closer to the scattering data.

The K-edge EXAFS of both constituents have been investigated in $Zr_{54}Cu_{46}$. The EXAFS results are shown in Fig.28 a) and b) respectively. Parts c) and d) show $|F(r)|$. In the $|F(r)|$ of the Zr EXAFS two well separated maxima show up at 2.2 Å and 2.8 Å, which can be ascribed to the Cu- and Zr-neighbours. The single Cu- and Zr-contributions in the Zr K-edge EXAFS have been isolated by inverse Fourier transform of each peak in $|F(r)|$ separately. Fits of $\chi_j(k)$ with Eq.22 using a nonsymmetric pair distribution (Eq.26 with a = 0.12 Å) for Cu and a Gaussian distribution for Zr neighbours yielded R- and N - values in good agreement with X-ray diffraction data [63] (see Table 4). In the Cu K-edge data only one broader maximum at 2.3 Å is observed, which has been attributed to both the Cu- and Zr-neighbours. An inverse Fourier transform of this peak yields the Cu- and Zr-contributions simultaneously. This EXAFS has been fitted by Eq.22 using R values of Zr-Cu as determined above and arg G(k) = 0. The significantly larger Cu-Cu distance found in X-ray diffraction again points to the fact that arg G(k) ≠ 0, i.e. to an asymmetric distribution. The coordination numbers are in agreement with the stoechiometric composition of the alloy but the pair distributions differ, i.e. symmetric for Zr-Zr and asymmetric for Cu-Cu and Cu-Zr.

6.3. Aqueous solution of $KMnO_4$ [64].

The contribution to the total absorption coefficient of $KMnO_4$ in aqueous solution due to excitations of Mn K-electrons is shown in Fig.29. The onset of the K-shell excitations is dominated by a sharp absorption line, which has been ascribed to transitions to a localized molecular orbital in the MnO_4^- ion.

The fine structure $\chi(k)$ and the magnitude of the Fourier transform $|F(r)|$ are shown in Fig.30 a and b. $|F(r)|$ is dominated by a peak at $r = 1.3$ Å, which represents the oxygen atoms surrounding the central Mn atom. To calculate bond lengths the phases $\Phi_i(k)$ of the Mn-O atom pair have been extracted from the experimental Mn K-absorption spectrum of MnO_2. According to the transferability of phases Φ_{MnO_2} and $\Phi_{MnO_4^-}$ are assumed to be identical. Then the difference of the Mn-O bond length in MnO_2 and MnO_4^- can be calculated from the total phases $\varphi(k) = 2kR + \Phi(k)$ according to

$$\Delta R(k) = (\varphi_{MnO_2}(k) - \varphi_{MnO_4^-}(k))/2k \qquad (43)$$

This function should be a constant over the whole k-range covered by the measurement. The most uncertain parameter for the calculation of ΔR is the zero of the kinetic energy E_o of the photoelectrons (see section 3). Therefore, E_o has been varied in Eq.2 to obtain a constant ΔR [10]. This variation certainly compensates the greater part of changes of the scattering phases at low kinetic energies of the photoelectrons in going from MnO_4^- to MnO_2. The result of this procedure is shown in Fig.31. Around an average value of $\Delta R = 0.231$ Å this function varies by less than $\pm 5 \cdot 10^{-3}$ Å. Together with the Mn-O distance of 1.88 Å in MnO_2 the absolute Mn-O bond length in MnO_4^- results in 1.649 Å $\pm$ 0.0005 Å

The amplitude functions A(k) of the contributions $\chi_1(k)$ due to the first scattering shells in MnO_2 and MnO_4^- have been used to check the coordination numbers. A plot of $\ln(A_{MnO_4^-}/A_{MnO_2})$ vs k^2 is shown in Fig.32. The deviations from a straight line at the boundaries of the k^2 region covered by the experiment are caused by window effects in the Fourier transform. The intersection with the vertical axis obtained from an extrapolation of the linear range determines the ratio of coordination numbers (A(k)~N). With 6 atoms in the first shell of

MnO_2 and a mean free path of the electrons of $\lambda = 6$ Å $\pm$ 2 Å and coordination numbers of $N_{MnO_4^-} = 4.05 \pm 0.10$ is obtained. For a Gaussian distribution ($A(k) \sim \exp(-2\sigma^2k^2)$) an increase of the mean square relative displacement of $\Delta\sigma^2 = 4 \cdot 10^{-3}$ Å^2 in going from MnO_4^- is calculated from the slope of the straight line.

6.4. Osmium-thiocyanate-complexes [14].

A structural analysis of the complexes $[Os(NCS)_n(SCN)_{6-n}]^{3-}$ available as salts of tetra-n-butylammonia has been reported by Rabe et al. [14]. Six of the seven possible complexes have been isolated by ion exchange chromatography [65]. From the intensities of groups of lines in the IR and Raman spectra characteristic for the S- and N-bonded (SCN)-group the sequence has been attributed to n = 1,2....6. Because of the complexity of this analysis independent criteria to confirm this assignment were desirable. Since it has not been possible to grow monocrystals with sufficient quality to determine the structure by X-ray diffraction, the EXAFS beyond the L_{III}-edge of Os has been analyzed to obtain the radial distribution around the absorbing Os atom.

The magnitude and the real part of the Fourier transform calculated from the experimental $k \cdot \chi(k)$ are shown in Fig.33. In the range $1.2 < r < 2.5$ Å two peaks are observed at $r_1 = 1.67$ Å and $r_2 = 2.06$ Å, which have been attributed to the nearest N and S neighbours respectively. As expected, the amplitude of the peak at r_1 decreases in going from n = 6 to n = 1, whereas the peak at r_2 shows the opposite behaviour. Two additional peaks in $|F(r)|$ of the sample with n = 6 at $r_3 = 2.68$ Å and $r_4 = 4.44$ Å are attributed to C and S atoms respectively. In going to $n < 6$ these peaks decrease. The $|F(r)|$ of the n = 1 sample is dominated by a single peak. The fact that the presence of the C and N atoms in this complex yields no significant contribution to $\chi(k)$

has been explained with a strong distortion of the OsS-CN bond angles. This leads to an effective spread of the Os-C and Os-N distances and consequently to a destructive interference in $\chi(k)$. Assuming an average bond angle of 105° it is concluded that in the complex n = 1 the OsS-CN bond angles vary by at least 10°.

An inverse Fourier transform over the range 1.25<r < 2.5 Å has been calculated, which represents a superposition of two contributions (nearest N and S neighbours of Os) to $\chi(k)$. The results of this transform are shown in Fig.34 as solid lines. To isolate each term and to calculate the bond lengths and coordination numbers of the individual N and S shells these data have been analyzed by a two shell fit using calculated amplitude functions and phase shifts [8, 66] and three free parameters for each shell (σ_j^2, R_j and an overall scaling factor p_j for the amplitudes). The best fits have been included in Fig.34 as dotted lines.

The interatomic distances determined in this way are summarized in Table 5. It is interesting to note that the Os-N bond length increases with decreasing number of N-bonded ligands, whereas the Os-S bond length of R = 2.50 Å remains unchanged within the experimental uncertainty of less than 0.01 Å.

The fitted scattering scaling factors p_j(j = N,S) are directly proportional to the coordination numbers N_j. In Fig.35 these values have been plotted vs n on the basis of the above mentioned assignments [65]. For a correct assignment the intersection of the linear regression p = An + B through the data points (solid lines) with the vertical axis at n = 0 should take the value B = 0. Changing the assignment by $\Delta n = 1$ would lead to $B = \pm A$. From the linear regressions $A_N = 0.165$, $B_N = -0.013$, $A_S = 0.047$ and $B_S = 0.012$ have been obtained. Both B values are significantly smaller than the A values which confirms that the sequence n = 1....6 has been isolated.

6.5 Structural investigation of a thin Cu film [38].

An analysis of the reflectance spectra of a 400 Å thick partially oxydized film of Cu to determine interatomic distances in superficial regions has been reported by Martens and Rabe [37, 38]. In order to extract structural information from the reflectivity one has to take into account the energy dependence of both the real and the imaginary part of the index of refraction $n = 1-\delta-i\beta$. Only β is proportional to the absorption coefficient μ. From the energy-(Fig.20) and the angular dependent reflectivities the optical constants β and δ have been extracted as discussed in detail in ref. [38]. Fig.36 shows δ as a function of the photon energy. On the left side of Fig.37 the EXAFS determined from the reflectance (ReflEXAFS) are shown for various glancing angles (c-h). For comparison the EXAFS of Cu_2O(a), CuO(b) and Cu(i) obtained from absorption measurements are included. With increasing glancing angles the fine structures derived from the reflection spectra change systematically.

At large glancing angles i.e. large penetration depths z (see Fig.21) the periodicity of the fine structures approaches the EXAFS of Cu.

The right hand side of Fig.37 shows the amplitudes of the Fourier transform of the fine structures. The Cu_2O and CuO transforms show two prominent peaks at 1.5 Å and 2.8 Å which represent the first oxygen and the second copper scattering shell around the central Cu atom. The transforms of the ReflEXAFS (Fig.37 c-h) only show one prominent peak around 2 Å with a small shoulder on the large distance side, which is the remainder of the second scattering shell in the oxide . With increasing glancing angle the main peak shifts to larger r values. The halfwidth decreases and the transforms approach that of pure Cu. The small shoulder at 3.3 $Å^{-1}$ in Fig.37 represents the second Cu shell in pure Cu. The peak around 4.2 Å in the Fourier transforms corresponds to the third scattering shell.

In Fig.38 the halfwidth of the peak around r = 2 Å is shown vs peak position. The solid line represents model calculations of the half width dependence for the superposition of two Gaussians with different relative amplitudes and half widths given by the peak at r = 1.5 Å in |F(r)| of CuO. In going from r = 2.18 Å to r = 1.5 Å in Fig.38 the width and position of the first Cu peak in |F(r)| of pure Cu (Fig.37i) changes to width and position of the first O peak in |F(r)| of CuO (Fig.37b). The relative number of Cu atoms surrounded by O atoms to that of all Cu atoms has been introduced as a scale of concentration of Cu oxide along this line.

From Fig.38 an integrated depth profile of the relative portion of Cu atoms surrounded by O atoms has been derived. This profile as function of the penetration depth z of the X-rays is shown in Fig.39. The concentration has been taken from Fig.38. The error bars have been estimated from the scatter of the experimental points. The dependence of the integrated concentration c on the penetration depth has been calculated under the assumption of a homogeneous overlayer of thickness d containing a mixture of c_o Cu atoms surrounded by O atoms and $(1-c_o)$ Cu atoms surrounded by Cu atoms. By integrating over the whole sample one obtains

$$c = c_o(1 - \exp(-d/z)) \qquad (44)$$

For $c_o = 0.8 \pm 0.05$ and a thickness of 85 Å ± 10 Å the calculated values follow the experimental data. This suggests that even in superficial regions Cu-Cu bonds exist, i.e. that the surface is only partially oxidized.

Acknowledgement

This report is based on joint efforts with W. Böhmer, G. Martens, N. Schwentner, G. Tolkiehn, and A. Werner, who deserve cordial thanks for a fruitful collaboration in the last years. Thanks are also due to Mrs. M. Höfelmeyer for a careful writing of the manuscript and Mrs. L. Bittner for preparing the photographs. The work was supported by the Deutsche Forschungsgemeinschaft DFG and the Bundesministerium für Forschung und Technologie BMFT.

References

1. B.M. Kincaid and P. Eisenberger, Phys.Rev.Letters 34, 1361 (1975)

2. P. Rabe, G. Tolkiehn, and A. Werner (unpublished results)

3. W. Böhmer and P. Rabe, J.Phys.C 12, 2465 (1979)

4. L.V. Azaroff and D.M. Pease, in X-ray Spectroscopy, ed. L.V. Azaroff (Mc.Graw Hill 1974), p. 284

5. P. Rabe, Jap.J.Appl.Phys. 17, Suppl.2, 22 (1978)

6. P.A. Lee and J.P. Pendry, Phys.Rev.B 11, 2795 (1975)

7. E.A. Stern, Phys.Rev.B 10, 3027 (1974)

8. B.-K. Teo and P.A. Lee, J.Am.Chem.Soc. 101, 2815 (1979)

9. P.H. Citrin, P. Eisenberger, and B.M. Kincaid, Phys.Rev. Letters 36, 1346 (1976)

10. G. Martens, P. Rabe, N. Schwentner, and A. Werner Phys.Rev.B 17, 1481 (1978)

11. P. Rabe, G. Tolkiehn, and A. Werner, J.Phys.C 12, 899 (1979)

12. A. Werner, Thesis, Universität Kiel 1979

13. N.F. Mott and H.S.W. Massey, The Theory of Atomic Collisions, (Clarendon Press, Oxford 1965)

14. P. Rabe, G. Tolkiehn, A. Werner, and R. Haensel, Z.Naturf. 34a, 1528 (1979)

15. S.P. Cramer, K.O. Hodgson, E.T. Stiefel, and W.E. Newton, J.Am.Chem.Soc. 100, 2748 (1978)

16. J.J. Rehr, E.A. Stern, R.L. Martin, and E.R. Davidson, Phys.Rev.B 17, 560 (1978)

17. P.A. Lee and G. Beni, Phys.Rev.B 15, 2862 (1977)

18. E.A. Stern, S.M. Heald, and B. Bunker, Phys.Rev.Letters 42, 1372 (1979)

19. E. Sevillano, H. Meuth, and J.J. Rehr, Phys.Rev.B 20, 4908 (1979)

20. P. Eisenberger and G.S. Brown, Sol.State Comm. 29, 481 (1979)

21. G. Martens, P. Rabe, N. Schwentner, and A. Werner, Phys.Rev.Letters 39, 1411 (1977)

22. R. Haensel, P. Rabe, G. Tolkiehn, and A. Werner, in Liquid and Amorphous Metals, ed E. Lüscher and H. Coufal (Sijthoff & Noordhoff Intern.Publ. 1980)

23. G.S. Brown, P. Eisenberger, and P. Schmidt, Sol.State Comm. 24, 201 (1977)

24. S.M. Heald and E.A. Stern, Phys.Rev.B 16, 5549 (1977)

25. S.M. Heald and E.A. Stern, Phys.Rev.B 17, 4069 (1978)

26. P. Rabe, G. Tolkiehn, and A. Werner, J.Phys.C 13,1857 (1980)

27. F.W. Lytle, D.E. Sayers, and E.A. Stern, Phys.Rev.B 11, 4825 (1975)

28. E.A. Stern, D.E. Sayers, and F.W. Lytle, Phys.Rev.B 11, 4836 (1975)

29. T.M. Hayes, P.N. Sen, and S.H. Hunter, J.Phys.C 9, 4357 (1976)

30. P. Rabe, G. Tolkiehn, and A. Werner, Nucl.Instr.Meth.

31. C. Kunz, ed. Synchrotron Radiation, Techniques and Applications, (Springer Verlag, 1979)

32. J.A. Del Cueto and N.J. Shevchik, J.Phys.E 11, 616 (1978)

33. G.S. Knapp, H. Chen, and T.E. Klippert, Rev.Sci.Instr. 49, 1658 (1978)

34. J.B. Hastings, B.M. Kincaid, and P. Eisenberger Nucl.Instr.Meth. 152, 167 (1978)

35. L.G. Parratt, C.F. Hempstead, and E.L. Jossem, Phys.Rev. 105, 1228 (1957)

36. J.J. Jaklevic, J.A. Kirby, M.P. Klein, A.S. Robertson, G.S. Brown, and P. Eisenberger, Sol.State Comm. 23, 679 (1977)

37. G. Martens and P. Rabe, phys.stat.sol.(a) 57, K 31 (1980)

38. G. Martens and P. Rabe, phys.stat.sol.(a)58(2), (1980)

39. P.A. Lee, Phys.Rev.B 13, 5261 (1976)

40. P.H. Citrin, P. Eisenberger, and R.C. Hewitt, Phys.Rev.Letters 41, 309 (1978)

41. J. Stöhr, L. Johansson, I. Lindau, and P. Pianetta Phys.Rev.B 20, 664 (1979)

42. G. Martens, P. Rabe, N. Schwentner, and A. Werner, J.Phys.C 11, 3125 (1978)

43. G. Martens, P. Rabe, G. Tolkiehn, and A. Werner, phys.stat.sol(a) 55, 105 (1979)

44. G. Martens, Diplomarbeit Universität Kiel 1977

45. C.N.J. Wagner, J.Non-Cryst.Sol. 31, 1 (1978)

46. N.J. Shevchik, Phil.Mag. 35, 805 (1977)

47. N.J. Shevchik, Phil.Mag. 35, 1289 (1977)

48. Y. Waseda and H.S. Chen, phys.stat.sol.(a) 49, 387 (1978)

49. P. Rabe, G. Tolkiehn, and A. Werner, J.Phys.C 12, L545 (1979)

50. R.G. Shulman, P. Eisenberger, and B.M. Kincaid, Ann.Rev.Biophys.Bioeng. 7, 559 (1978)

51. S.I. Chan, V.W. Hu, and R.C. Gamble, J. Molec.Struct. 45, 239 (1978)

52. S.P. Cramer and K.O. Hodgson, Progr.Inorg.Chem. 25, 1 (1979)

53. S. Doniach, P. Eisenberger, and K.O. Hodgson in Synchrotron Radiation Research, ed.s H. Winick and S. Doniach (Plenum Press, New York, 1980)

54. T.M. Hayes, J.Non-Cryst.Sol. 31, 57 (1978)

55. G. Lucovsky and T.M. Hayes, in Amorphous Semiconductors ed. H.H. Brodsky, Topics of Applied Physics Vol.36 (Springer Verlag, 1979) p.215

56. F.W. Lytle, G.H. Via, and J.H. Sinfeld, in Synchrotron Radiation Research, ed.s H. Winick and S. Doniach (Plenum Press, New York, 1980)

57. J.B. Boyce and T.M. Hayes, in Physics of Superionic Conductors, ed. M.B. Salamon, Topics in Current Physics, Vol.15 (Springer Verlag, Berlin 1979), p.5

58. D.E. Sayers, E.A. Stern, and F.W. Lytle, Phy.Rev.Letters 27, 1204 (1971)

59. J. Tauc, Amorphous and Liquid Semiconductors,(Plenum Press, 1974)

60. D.E. Polk, J.Non-Cryst.Sol. 5, 365 (1971)

61. N.J. Shevchik and W. Paul, J.Non-Cryst.Sol. 8-10, 381 (1972)

62. J.L. Finney, Proc.Roy.Soc. 319A, 479 (1970)

63. H.S. Chen and Y. Waseda, phys.stat.sol.(a) 51, 593 (1979)

64. P. Rabe, G. Tolkiehn, and A. Werner, J.Phys.C 12, 1173 (1979)

65. W. Preetz and G. Peters, Z.Naturf. 34b, 1243 (1979)

66. B.-K. Teo, P.A. Lee, A.L. Simons, P. Eisenberger, and B.N. Kincaid, J.Am.Chem.Soc. 99, 3854 (1977)

Table 1: Reduction factors S_o^2 for EXAFS amplitudes due to relaxation of the central atom [16].

	F	Cl	Br
atom	0.74	0.71	0.72
molecule	0.60	0.64	0.64

Table 2: (a) Variation of the mean-square relative displacements σ^2 with temperature for the nearest (I) and next-nearest (II) neighbours in crystalline and amorphous Ge. (b) Differences in σ^2 for a-Ge (I), c-Ge (I) and c-Ge (II) at 80 K [49].

	$\Delta\sigma^2$ (10^{-2} Å^2)		
	80 - 300 K	80 - 400 K	80 k
(a)			
c-Ge (I)	0.04 ± 0.02	0.07 ± 0.02	
c-Ge (II)	0.45 ± 0.02	0.63 ± 0.05	
a-Ge (I)	0.22 ± 0.02	0.28 ± 0.02	
(b)			
a-Ge (I) - c-Ge (I)			0.26 ± 0.02
a-Ge (I) - c-Ge (II)			0.21 ± 0.03
c-Ge (II) - c-Ge (I)			0.05 ± 0.03

Table 3: Structural parameters for the nearest neighbours of Fe in $Fe_{80}B_{20}$ [22].

Shell	R_E(Å)	N_E	σ_E^2(Å^2)	R_E^c(Å)	N_E^c	R_D(Å)	N_D
B	1.96	1.2	0.009	2.06	2.2		
Fe	2.46	4.5	0.010	2.55	8.22	2.57	1.19

E : after parameter fit using a Gaussian distribution

c : after correcting for the asymmetric distribution

D : X-ray diffraction data [48]

Table 4: Structural parameters of $Zr_{54}Cu_{46}$ [22].

Central atom	Scatterer	R_E (Å)	N_E	R_D(Å)	N_D
Zr	Cu	2.74 ± 0.02^c	4.6 ± 1^c	2.75	5.0
	Zr	3.14 ± 0.02	5.1 ± 1	3.15	5.0
Cu	Cu	2.47 ± 0.03		2.53	5.8
	Zr	2.74 ± 0.03^c		2.75	5.6

E,c: see table 3; D: X-ray diffraction data [63]

Table 5: Interatomic distances R_N and R_S between the central Os atom and the next N and S neighbours in $[Os(NCS)_n(SCN)_{6-n}]^{3-}$ [14].

n	R_N	R_S
6	2.13	-
5	2.13	2.50
3	2.16	2.50
2	2.21	2.50
1	2.21	2.51

Figure captions

1. Absorption coefficient of atomic Kr at the K-edge [1].
2. Absorption coefficient of ferrocene at the Fe K-edge [2].
3. Absorption coefficient of polycrystalline Cu at the K-edge [3].
4. Schematic description of the absorption process:
   a) Potentials of the absorbing and scattering atoms with K- and L-levels; R radial distance; E_o zero of the kinetic energy E_{kin} scale of the photoelectrons; $\hbar\omega$ photon energy;
   b) Relation between E_{kin} and λ of the photoelectron wave;
   c) Outgoing (solid line) and backscattered (dashed line) electron wave; the hatched areas symbolize the K-level wavefunction.
5. a) and b) experimental scattering amplitudes kA(k) normalized to R = 1 Å and N = 1 [2, 11, 12]; the dotted lines in b) are theoretical values [8].
6. Comparison of the positions of the maxima and minima of calculated (dots [8]) and experimental (circles [2]) scattering amplitudes. The lines represent the trends of the theoretical values.
7. Comparision of calculated (dots and circles [8]) and experimental scattering phases Φ (solid lines [11]) for Cu and Au.
8. Calulated amplitudes of the EXAFS of Cu caused by multiple scattering[6].
9. Magnitude $|F(r)|$ and real part Re F(r) of the Fourier transform of the Cu K-edge EXAFS. Note the sign reversal of Re F(r) of the fourth shell contribution compared to Re F(r) of the first three shells introduced by multiple scattering [12].
10. Correlation function γ (Eq.21) calculated for various temperatures T (q_D Debye wave number, Θ Debye temperature, R interatomic distance). The arrows indicate the first 13 shells in a fcc lattice [3].
11. Temperature dependence of the mean square relative displacements σ^2 for the first (1) and second neighbours (2) in Co, Cu, RbCl, and SrS calculated with Eq.s 19-21. The EXAFS results (bars) have been fitted to the σ^2 calculated for T = 80 K [3].
12. Beats caused by close lying shells: a) Model EXAFS for two shells with c = 1 (Eq. 22) and R = 0.3 Å; b) Fourier transform of (a); c) amplitudes $|f_1||G_1| / |f||G|$ (Eq. 23) and phases $\Phi + \arg G$ for various constant parameters c with $\Delta\Phi = 0$ and $\Delta \arg G = 0$ [5,21].
13. Magnitude of the Fourier transform G(k) and $\Delta R(k) = (2k)^{-1} \arg G(k)$ calculated from Eq.12 with an asymmetric pair distribution (Eq.26) [12, 22].
14. Schematic arrangement for the investigation of the anisotropy of EXAFS of a GeS single crystal (a,b,c crystal axes; Ge: central atom; S, Ge: scattering atoms; ε polarization vector [26].
15. EXAFS k χ(k) above the K-edge of Ge in monocrystalline GeS for polarization directions $\varepsilon \| a$ and $\varepsilon \| c$. The bars in |F(r)| symbolize the contributions to be expected from the known crystal structure (solid bars: S scatterers; dotted bars: Ge scatterers [26].
16. Experimental setup for EXAFS measurements at DESY (LS lead slit, CR crystal, IC ionization chamber, S sample, GO goniometer, LT lifting table, C current amplifier, VF voltage to frequency converter)[5].
17. Schematic comparison of the properties of an X-ray tube and synchrotron radiation.
18. Comparison of intensities of the bremsstrahlung of a Cu-anode and synchrotron radiation of DESY [30].
19. Ratio of measured (χ_m) to actual (χ) EXAFS amplitudes as a function of the inhomogeneity R of the sample thickness. R is the percentage of the sample

area (assumed homogeneous thickness) covered by holes. The values were calculated for different values μd, for $E > E_K$ (E_K: K absorption edge energy) and a ratio of absorption coefficients $\mu (E < E_K) / \mu (E > E_K) = 0.155$ (a typical case for Cu) [30].

20. Reflectivity of a Cu film (d = 400 Å) on glass vs photon energy in the vicinity of the Cu K-edge for different glancing angles of incidence [38].
21. Penetration depth z of X-rays in a Cu surface for two wavelengths above and below the K-edge (λ_K = 1.38 Å) and the respective optical constants [38].
22. Comparison of Ni EXAFS by a) absorption, and total photoelectron yield of a b) polycrystalline surface, c) (111) surface [43].
23. Photoelectron yield as a function of the glancing angle φ normalized to the yield at $\varphi = 90^\circ$ [44].
24. Comparison of the EXAFS $\chi(k)$ of $Fe_{80}B_{20}$ at the Fe K-edge with S(Q) determined from X-ray diffraction [48]; from [22].
25. Experimental σ^2 for c-Ge (x nearest, + next-nearest neighbours) and a-Ge (o nearest neighbours) as a function of T. The temperature dependence of the mean square relative displacement calculated within the Debye approximation is included for nearest (-·-·-), next nearest (- - -) neighbours and for uncorrelated (———) atoms [49].
26. EXAFS $\chi(k)$ of $Fe_{80}B_{20}$ in the vicinity of the Fe K-edge and the Fourier transform $|F(r)|$ [22].
27. a) Solid line: Backtransform of the first maximum in the $|F(r)|$ of $Fe_{80}B_{20}$ of Fig.26; dots: two shell fit (Fe and B); b) single shell contributions separated by the parameter fit [22].
28. EXAFS of amorphous $Zr_{54}Cu_{46}$ above the Zr (a) and Cu (b) K-edges; c) and d) show the $|F(r)|$ of a) and b) resp. [22].
29. Mn K-absorption spectrum of a 0.4 m aqueous solution of $KMnO_4$ [64].
30. EXAFS (a) and $|F(r)|$ (b) calculated from the spectrum in Fig.29 [64].
31. Difference ΔR of the interatomic Mn-O distances in MnO_2 and MnO_4^- (in solution) according to Eq.43 [64].
32. Logarithm of the ratio of the amplitude functions A(k) for the nearest neighbours of Mn in MnO_4^- (solution) and MnO_2. The value for $k^2 = 0$ gives $N_{MnO_4^-} / N_{MnO_2} = 0.675$, the slope yields the variation of the mean square relative displacements $\sigma^2_{MnO_2} - \sigma^2_{MnO_4^-} = 4 \cdot 10^{-3}$ Å^2 [64].
33. Magnitude $|F(r)|$ and real part Re F(r) of the Fourier transform of the EXAFS of $[Os(NCS)_n(SCN)_{6-n}]^{3-}$ above the Os L_{III} edge [14].
34. Contribution to the EXAFS by the next neighbours (N,S) of the central Os-atom. Solid lines: result of the inverse Fourier transform of the range 1.2 Å < r < 2.5 Å in Fig.33; dotted lines: fits with calculated scattering amplitudes and phases [14].
35. Dots: parameter p_N and p_S for N and S neighbours obtained from the fit of the filtered EXAFS (Fig.34). The p_j are proportional to the number of N- and S- neighbours; Solid lines: linear regression through the experimental points [14].
36. Measured energy dependence of the unit decrement δ of the real part of the index of refraction. The deviation of the measured points from the smooth line above the K-edge energy represent EXAFS. The insert shows δ in an expanded scale [38].
37. Left side: EXAFS of a) Cu_2O, b) CuO and i) Cu taken by absorption measurements. EXAFS extracted from the energy and angular dependent reflectance for the glancing angles of c) 0.210°, d) 0.260°, e) 0.285°, f) 0.310°, g) 0.335° and h) 0.360°. Right side: $|F(r)|$ of the corresponding fine structures [38].

38. Model calculations of the half width and peak position dependence of Fourier peaks as a function of the relative number of Cu atoms surrounded by O atoms presented as oxide concentration c along the solid line. The points are taken from the first peak of |F(r)| in Fig.36 b) to i) [38].

39. Integrated depth profile of the relative number of Cu atoms surrounded by O atoms near the surface of the sample [38].

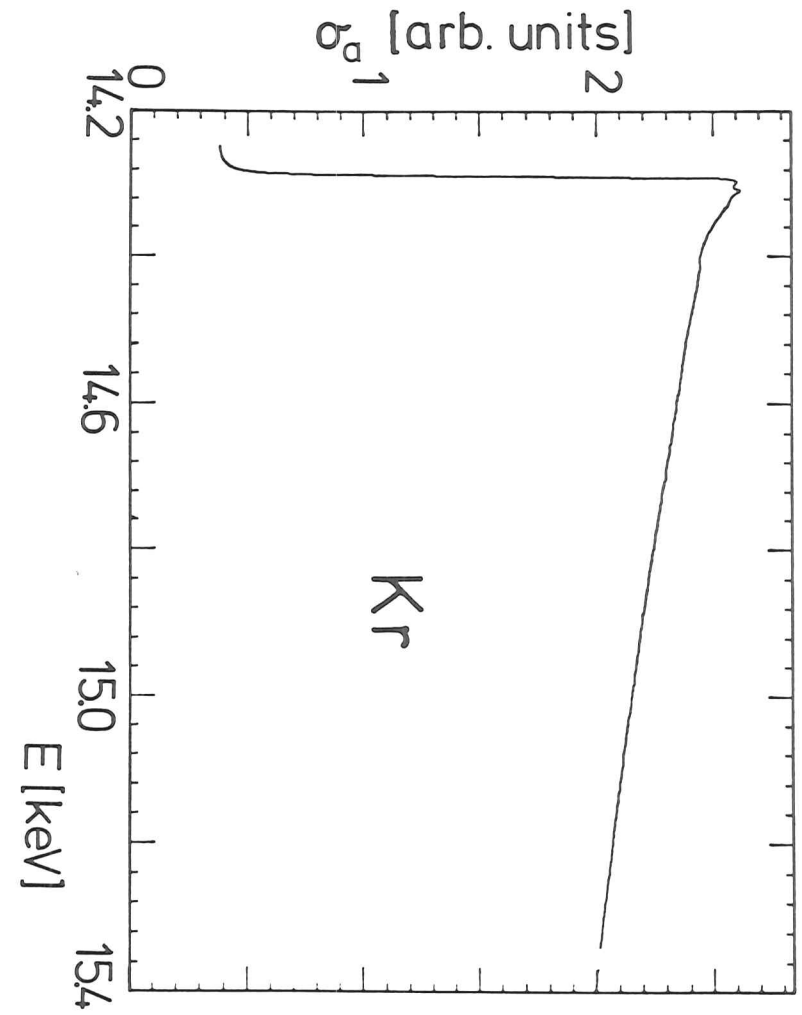

Fig. 1

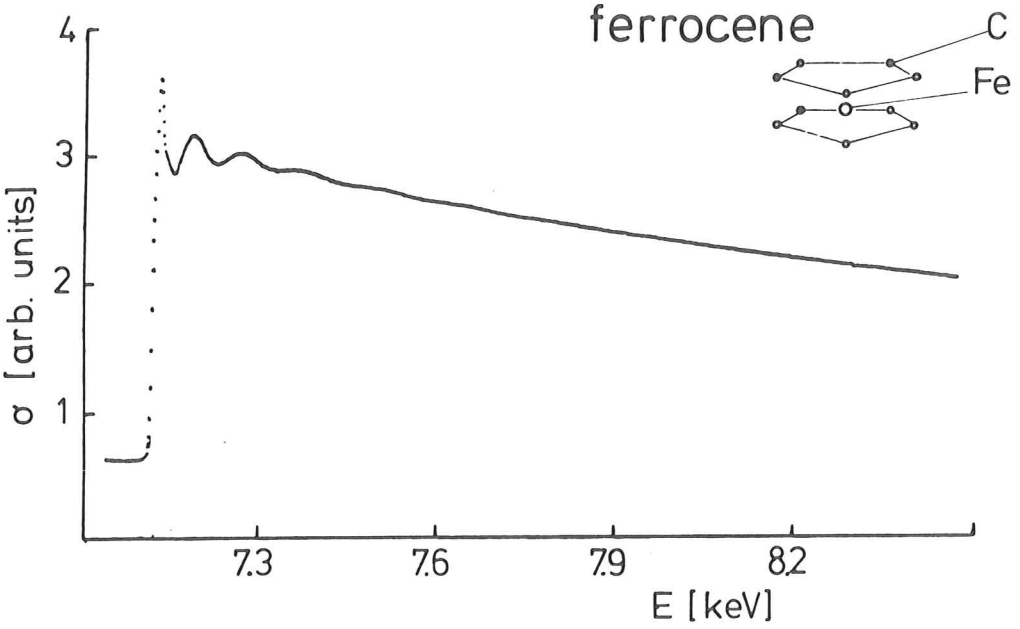
ferrocene
C
Fe
σ [arb. units]
4
3
2
1
7.3
7.6
7.9
8.2
E [keV]

Fig. 2

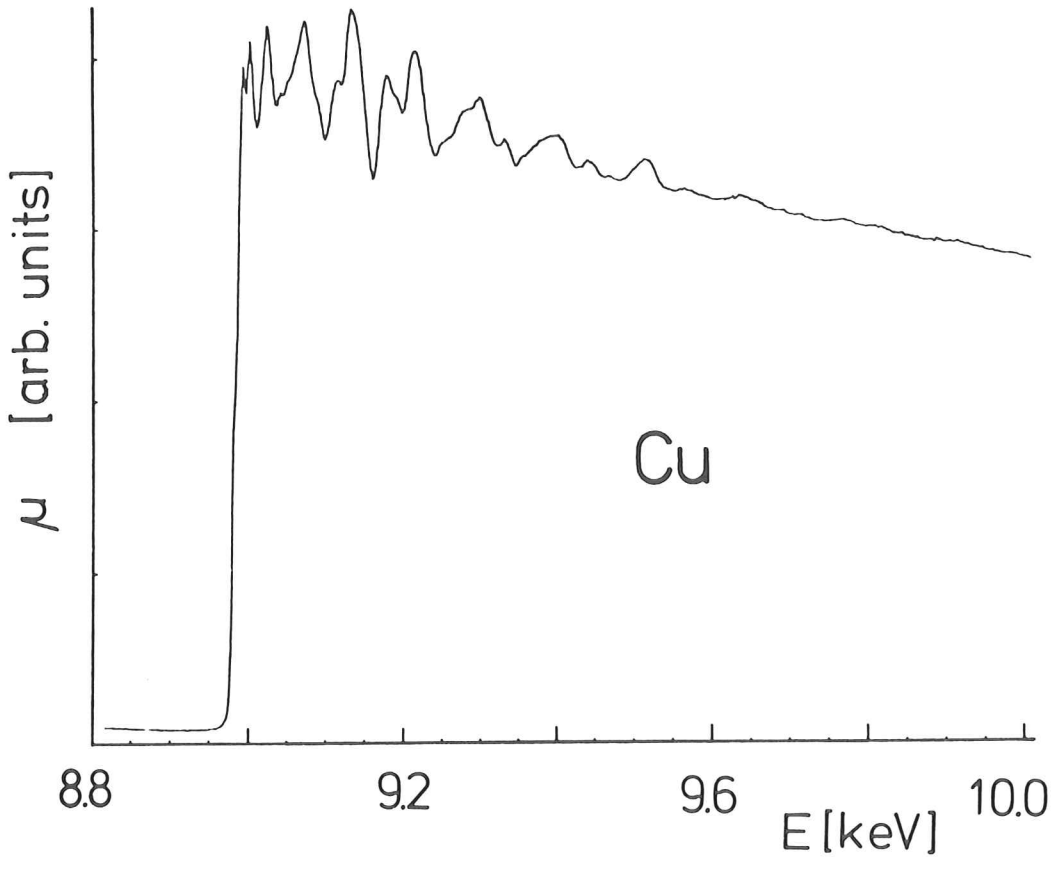
μ [arb. units]
Cu
8.8
9.2
9.6
10.0
E [keV]

Fig. 3

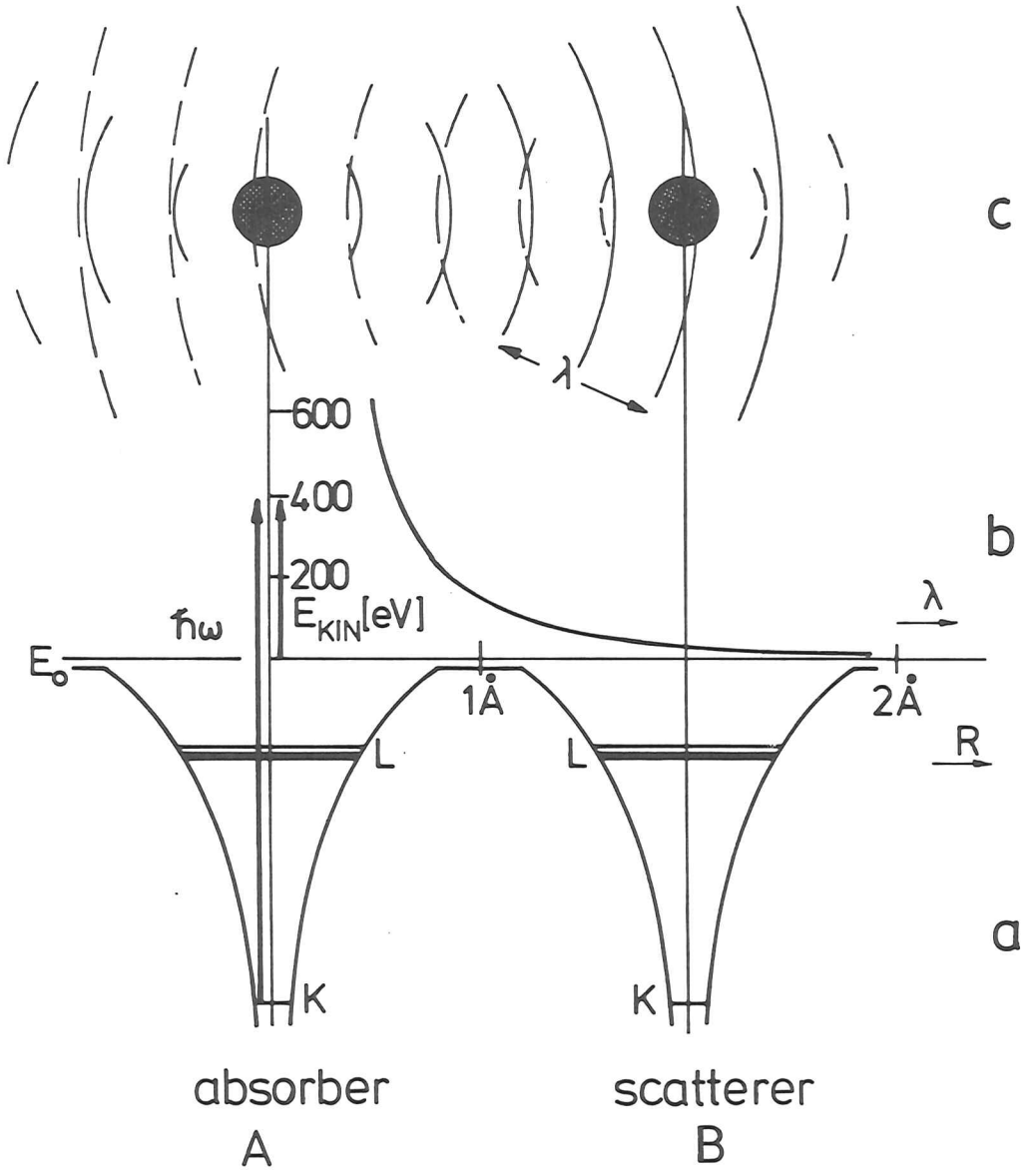
c
b
a
λ
600
400
200
E_KIN[eV]
ħω
E_o
1Å
2Å
λ
R
L
L
K
K
absorber
A
scatterer
B

Fig. 4

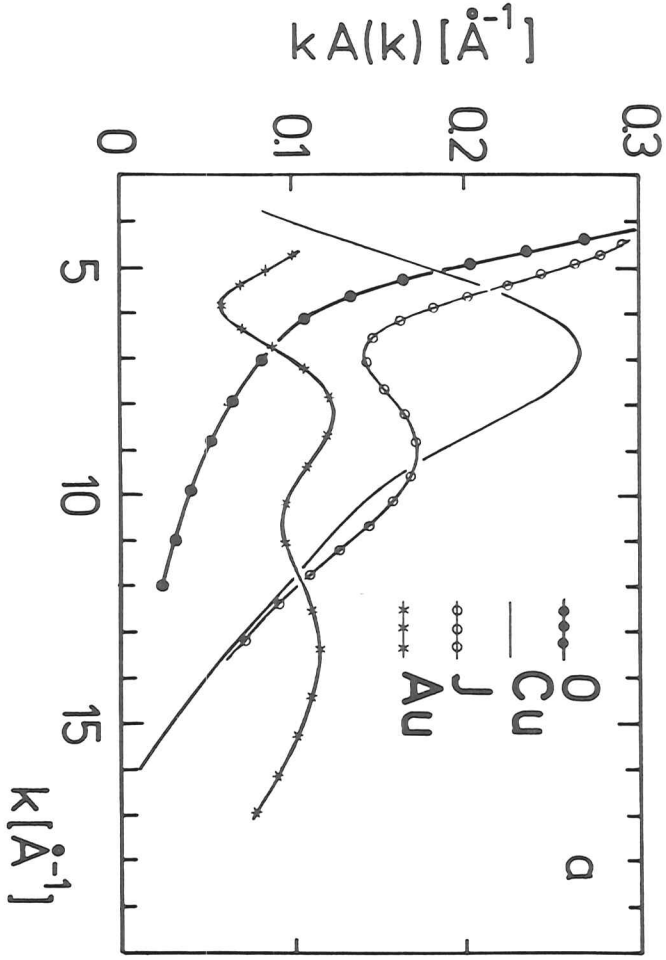
kA(k) [Å^-1]
0
0.1
0.2
0.3
5
10
15
k[Å^-1]
O
Cu
J
Au
a

Fig. 5a

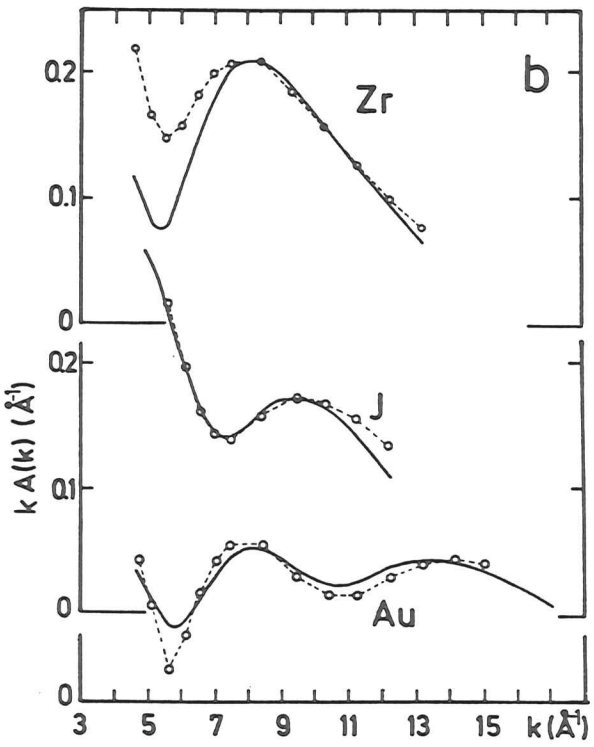
b
Zr
J
Au
0.2
0.1
0
k A(k) (Å⁻¹)
3
5
7
9
11
13
15
k (Å⁻¹)

Fig. 5b

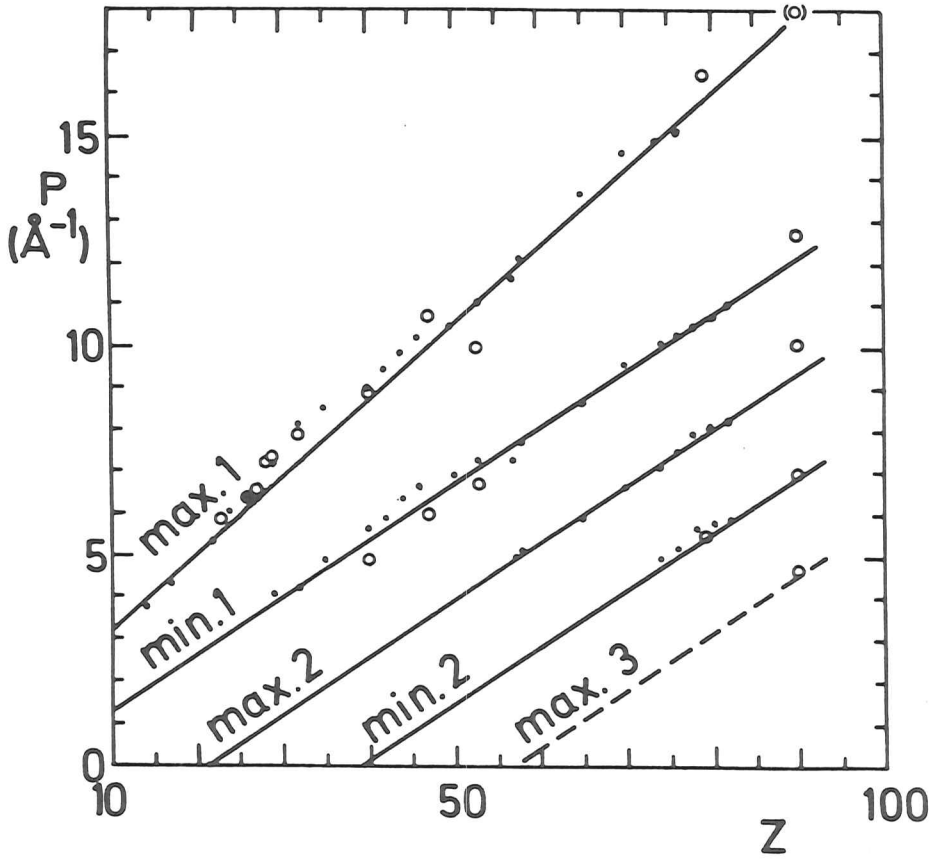
P
(Å⁻¹)
15
10
5
0
max.1
min.1
max.2
min.2
max.3
10
50
100
Z

Fig. 6

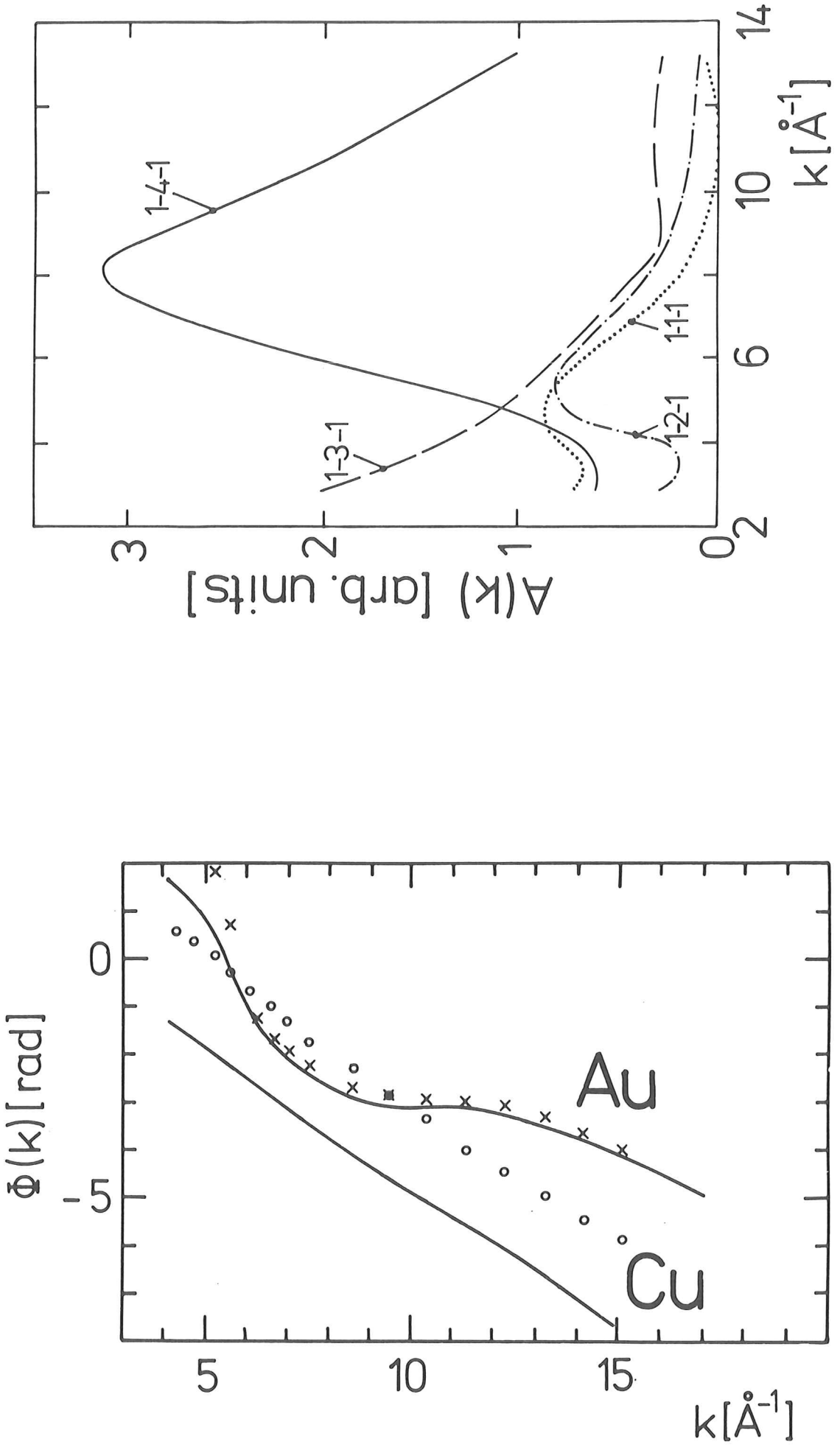

Fig. 8

Fig. 7

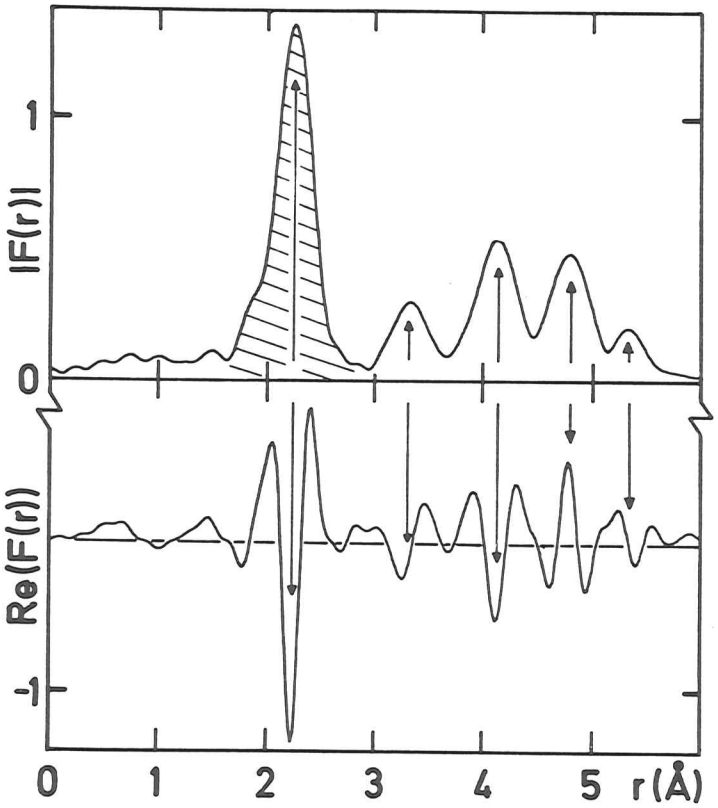

Fig. 9

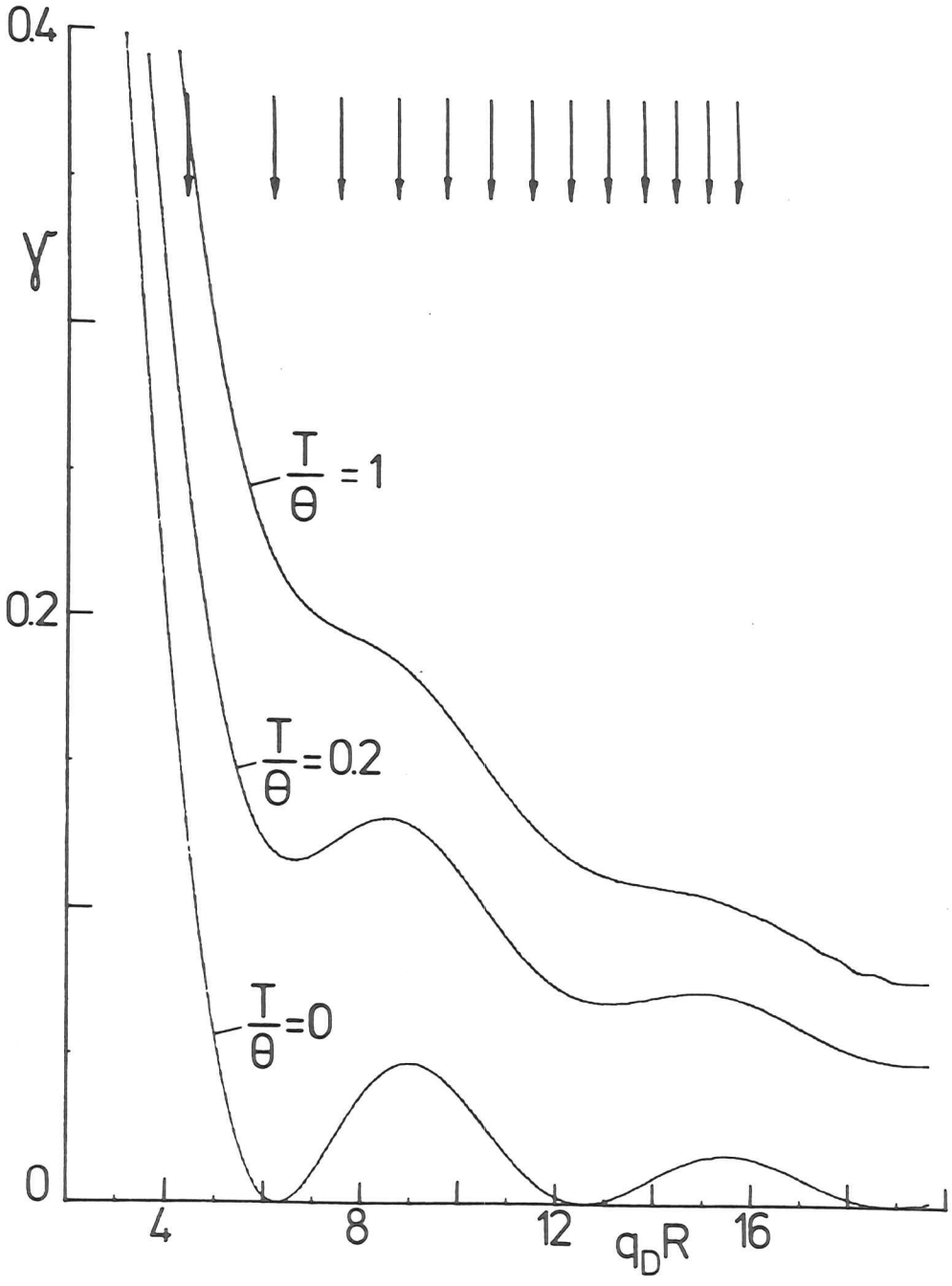

Fig. 10

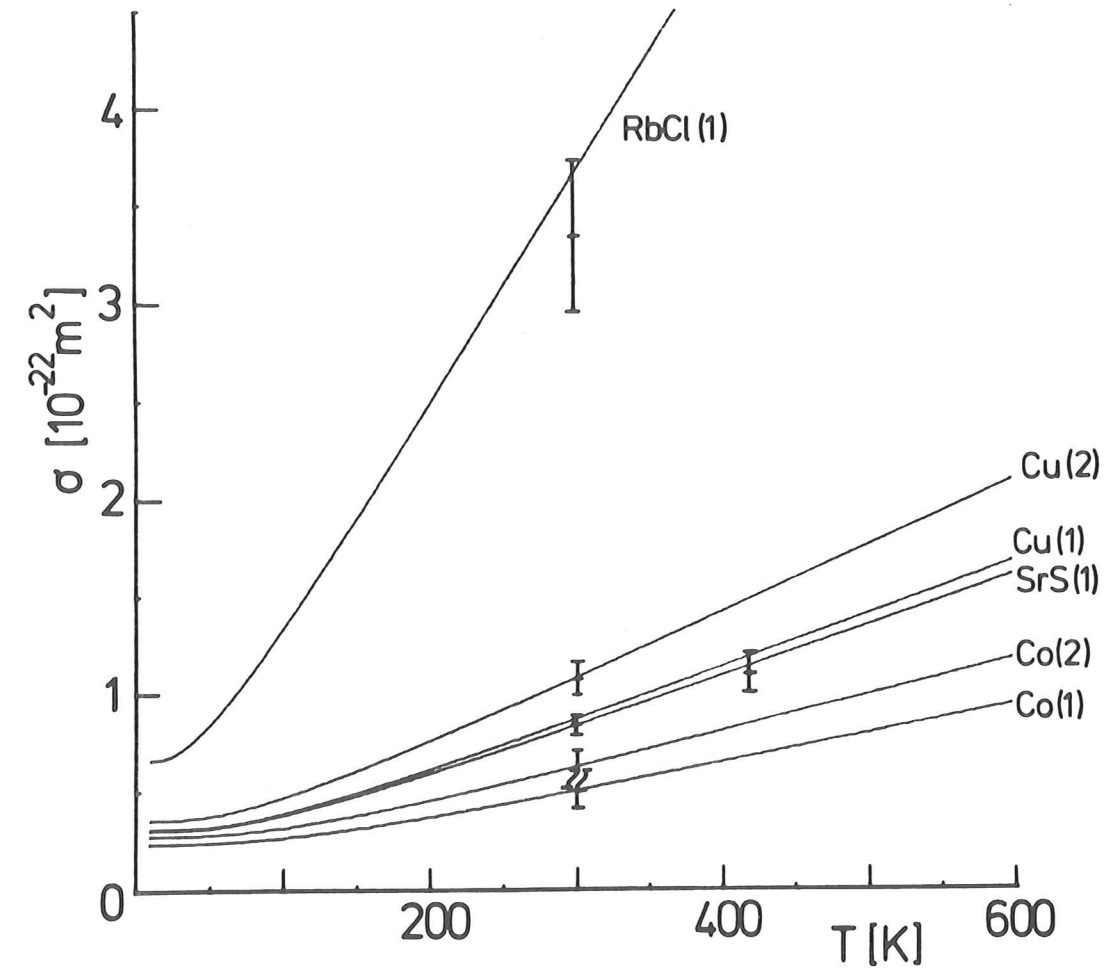
RbCl (1)
Cu(2)
Cu(1)
SrS(1)
Co(2)
Co(1)
σ [10^-22 m^2]
T [K]
0
1
2
3
4
200
400
600

Fig. 11

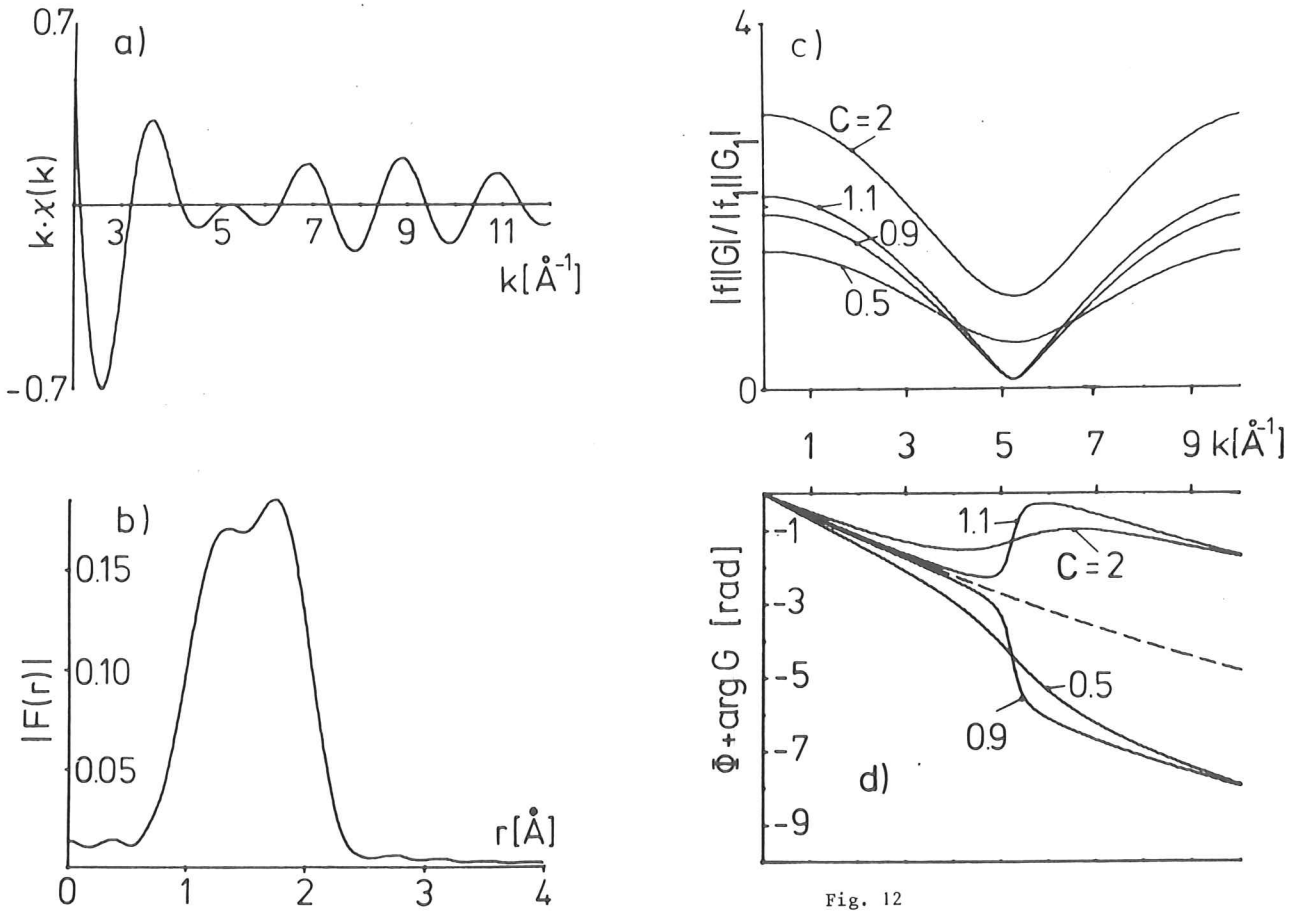
a)
k·χ(k)
k[Å^-1]
0.7
-0.7
3
5
7
9
11
b)
|F(r)|
r[Å]
0.15
0.10
0.05
0
1
2
3
4
c)
|f||G|/|f1||G1|
C=2
1.1
0.9
0.5
1
3
5
7
9 k[Å^-1]
Φ+arg G [rad]
1.1
C=2
0.5
0.9
d)
-1
-3
-5
-7
-9

Fig. 12

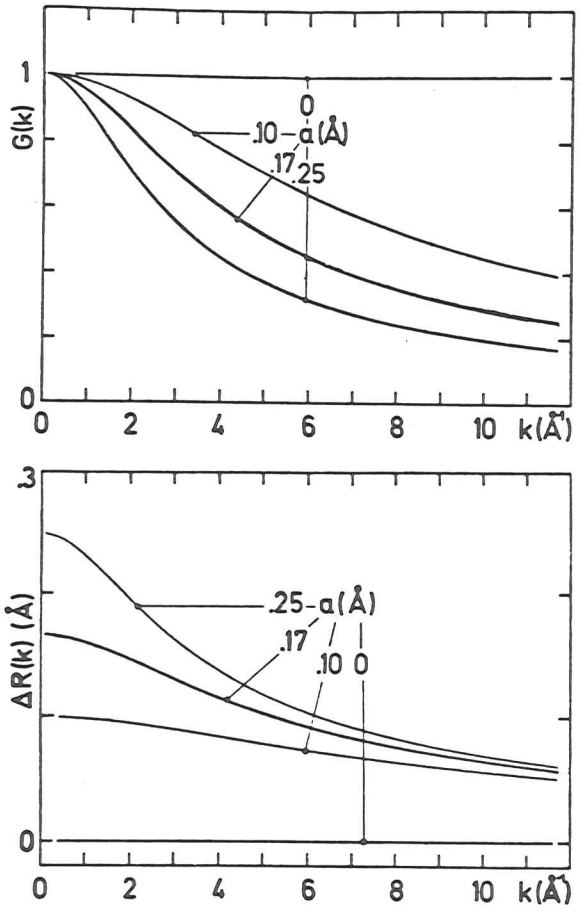
G(k)
1
0
0
.10
.17
.25
a(Å)
0
2
4
6
8
10
k(Å⁻¹)
ΔR(k) (Å)
.3
0
.25
.17
.10
0
a(Å)
0
2
4
6
8
10
k(Å⁻¹)

Fig. 13

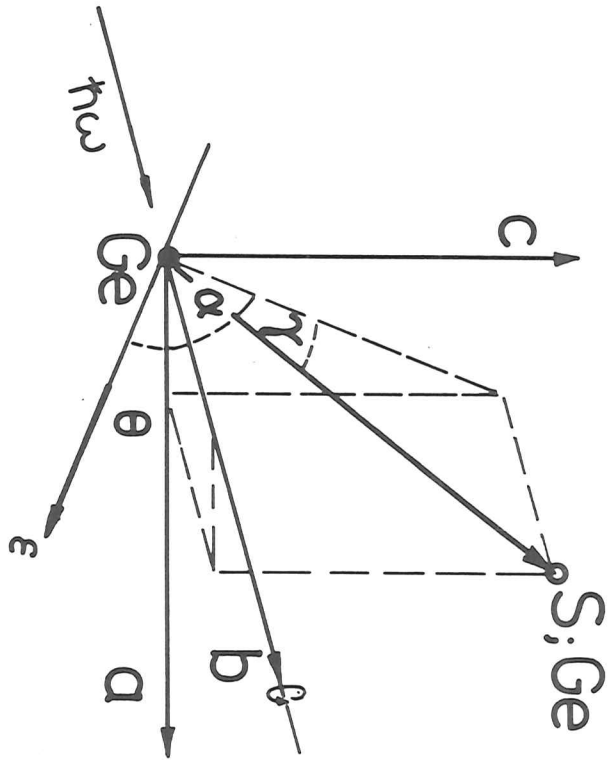
ħω
Ge
c
α
γ
θ
3
a
b
S;Ge

Fig. 14

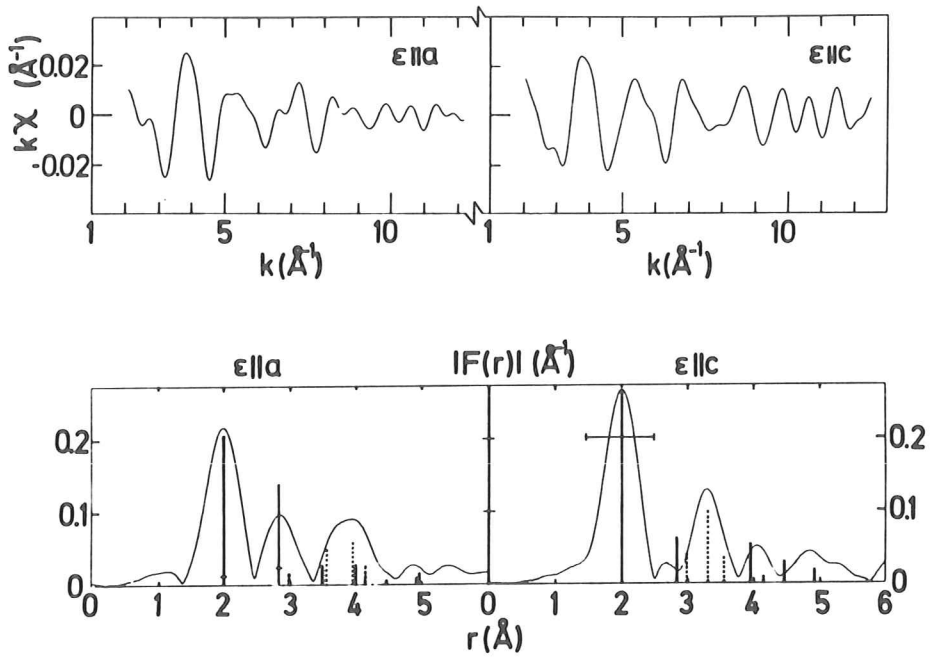
ε⊥a
ε∥c
kχ (Å⁻¹)
0.02
0
-0.02
1
5
10
k(Å⁻¹)
|F(r)| (Å⁻¹)
0.2
0.1
0
0 1 2 3 4 5
r(Å)

Fig. 15

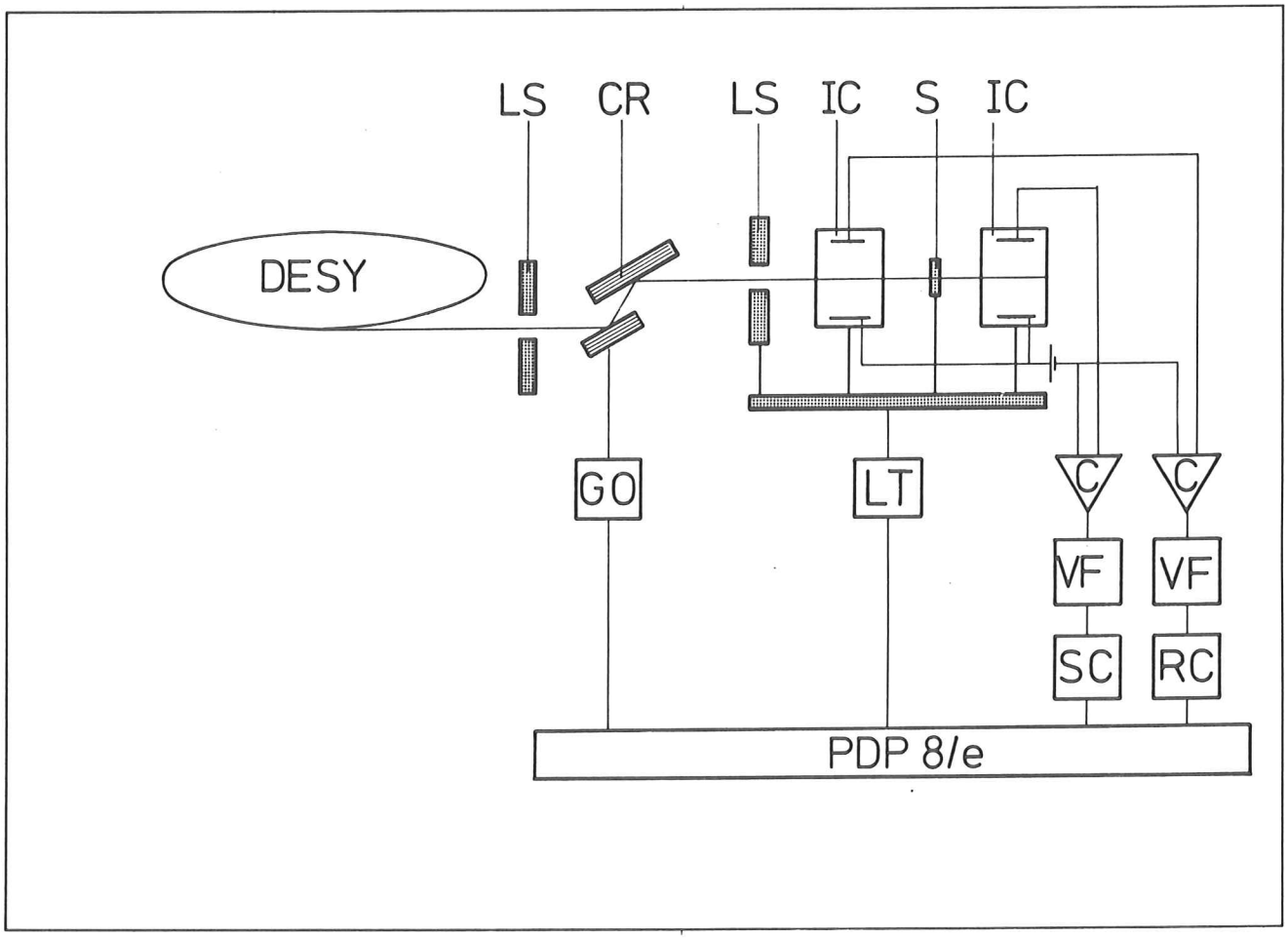
LS
CR
LS
IC
S
IC
DESY
GO
LT
C
C
VF
VF
SC
RC
PDP 8/e

Fig 16

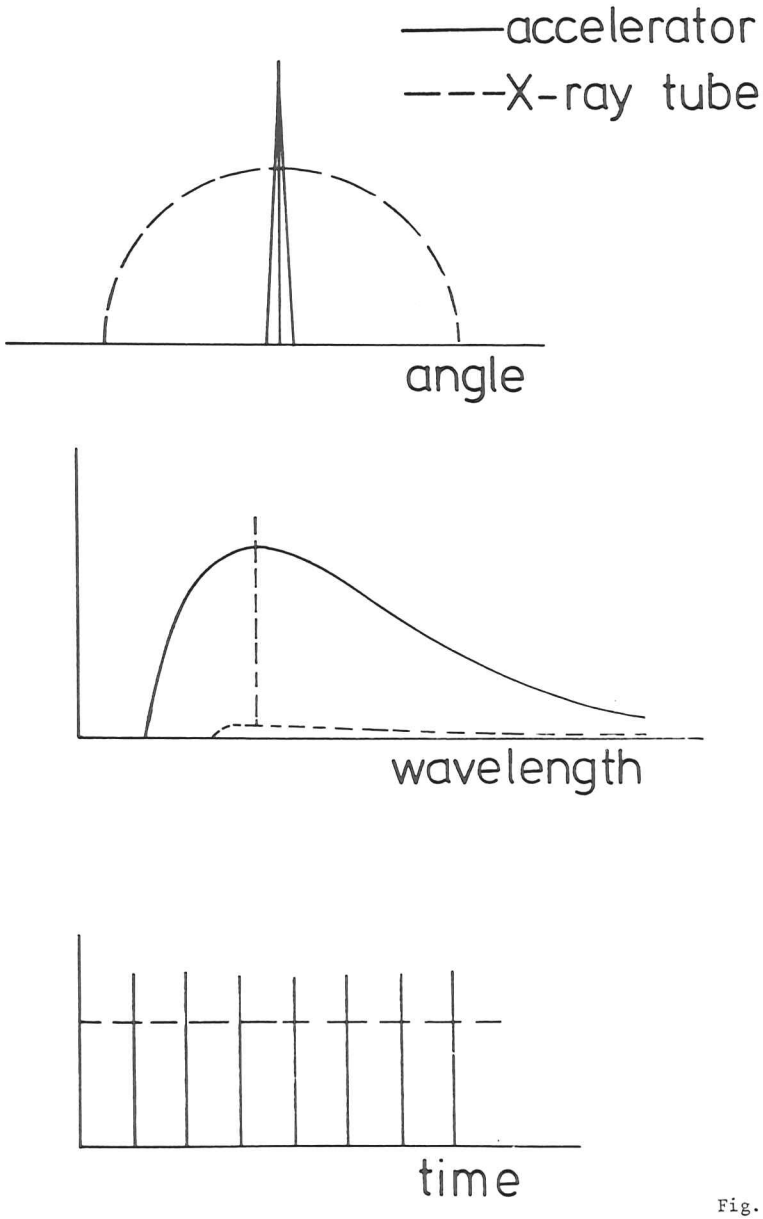
——accelerator
---X-ray tube
angle
wavelength
time

Fig. 17

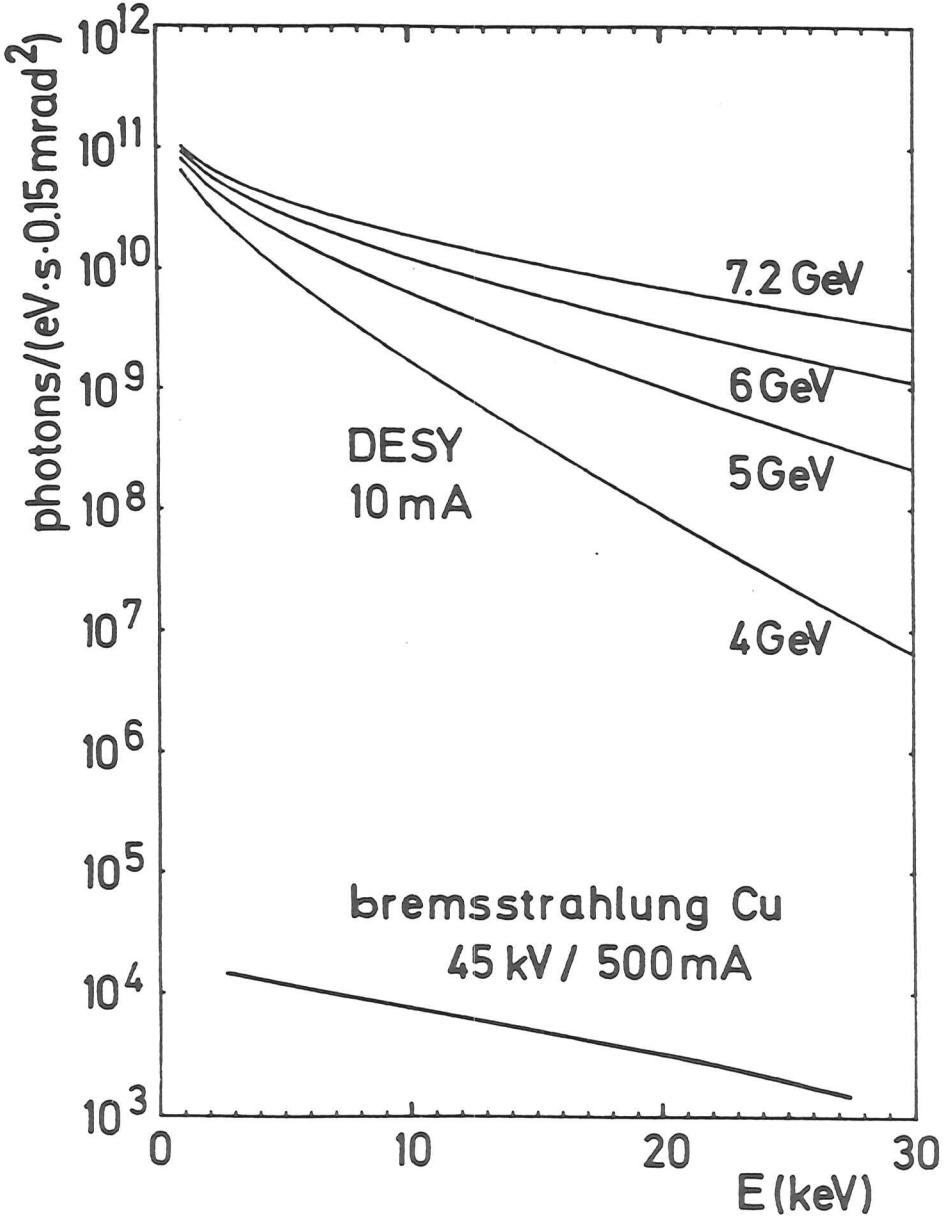
photons/(eV·s·0.15mrad²)
10¹²
10¹¹
10¹⁰
10⁹
10⁸
10⁷
10⁶
10⁵
10⁴
10³
0
10
20
30
E(keV)
7.2 GeV
6 GeV
5 GeV
4 GeV
DESY
10 mA
bremsstrahlung Cu
45 kV / 500 mA

Fig. 18

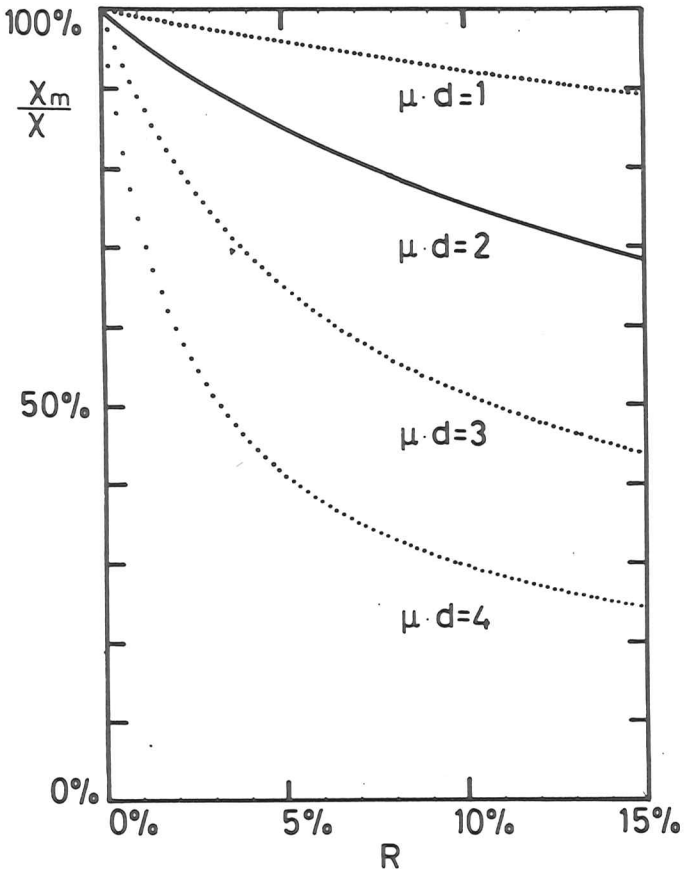
100%
Xm/X
μ·d=1
μ·d=2
μ·d=3
μ·d=4
50%
0%
0%
5%
10%
15%
R

Fig. 19

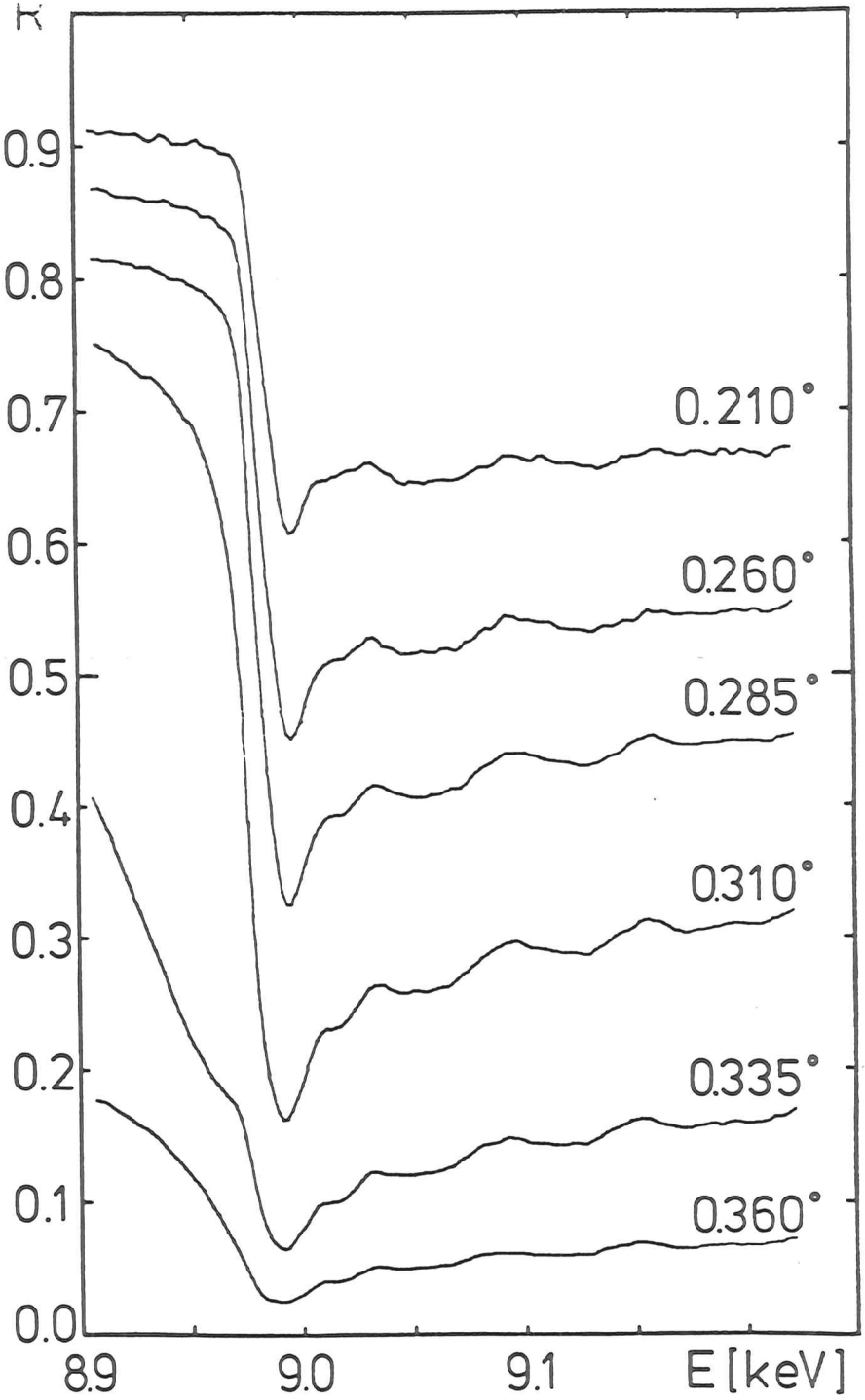
R
0.9
0.8
0.7
0.6
0.5
0.4
0.3
0.2
0.1
0.0
0.210°
0.260°
0.285°
0.310°
0.335°
0.360°
8.9
9.0
9.1
E [keV]

Fig. 20

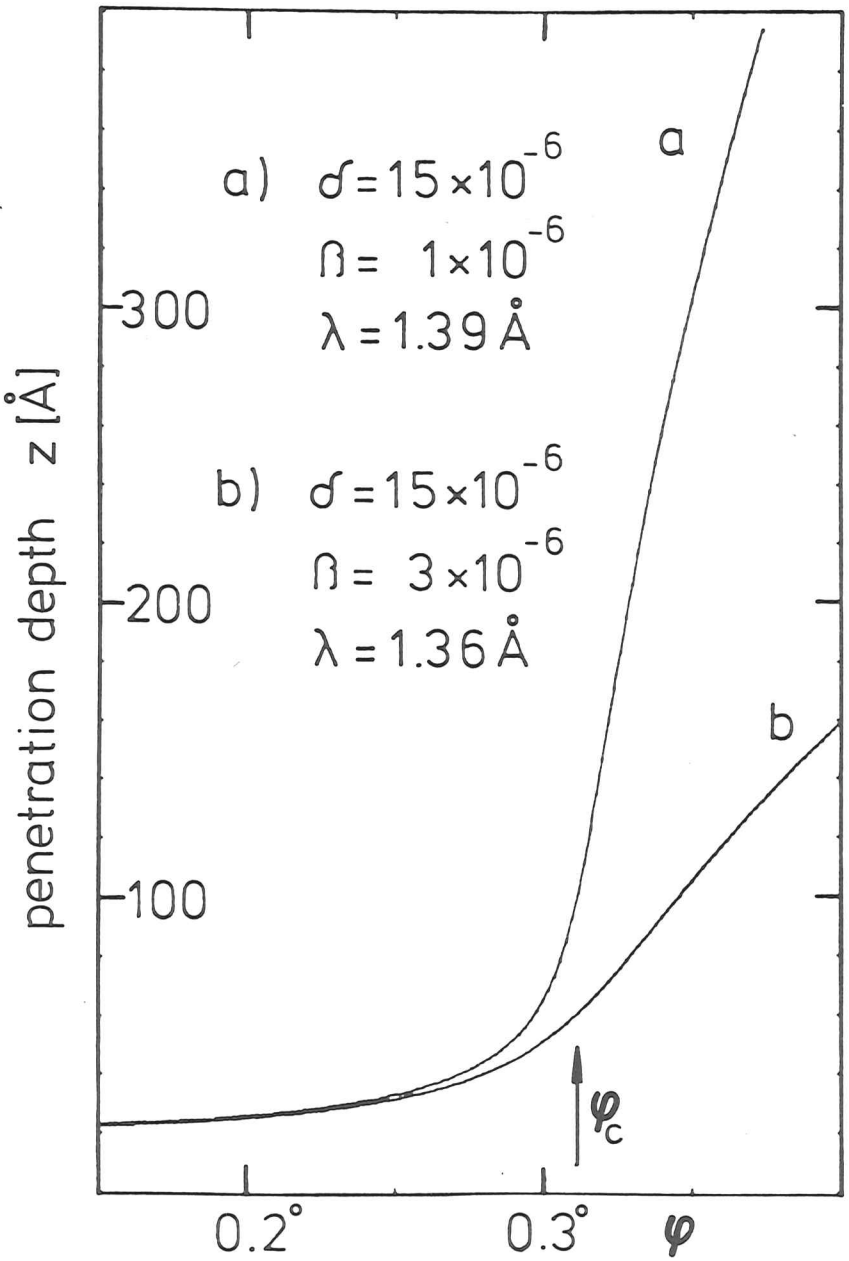
penetration depth z [Å]
300
200
100
a) δ = 15×10⁻⁶
β = 1×10⁻⁶
λ = 1.39 Å
b) δ = 15×10⁻⁶
β = 3×10⁻⁶
λ = 1.36 Å
a
b
φc
0.2°
0.3°
φ

Fig. 21

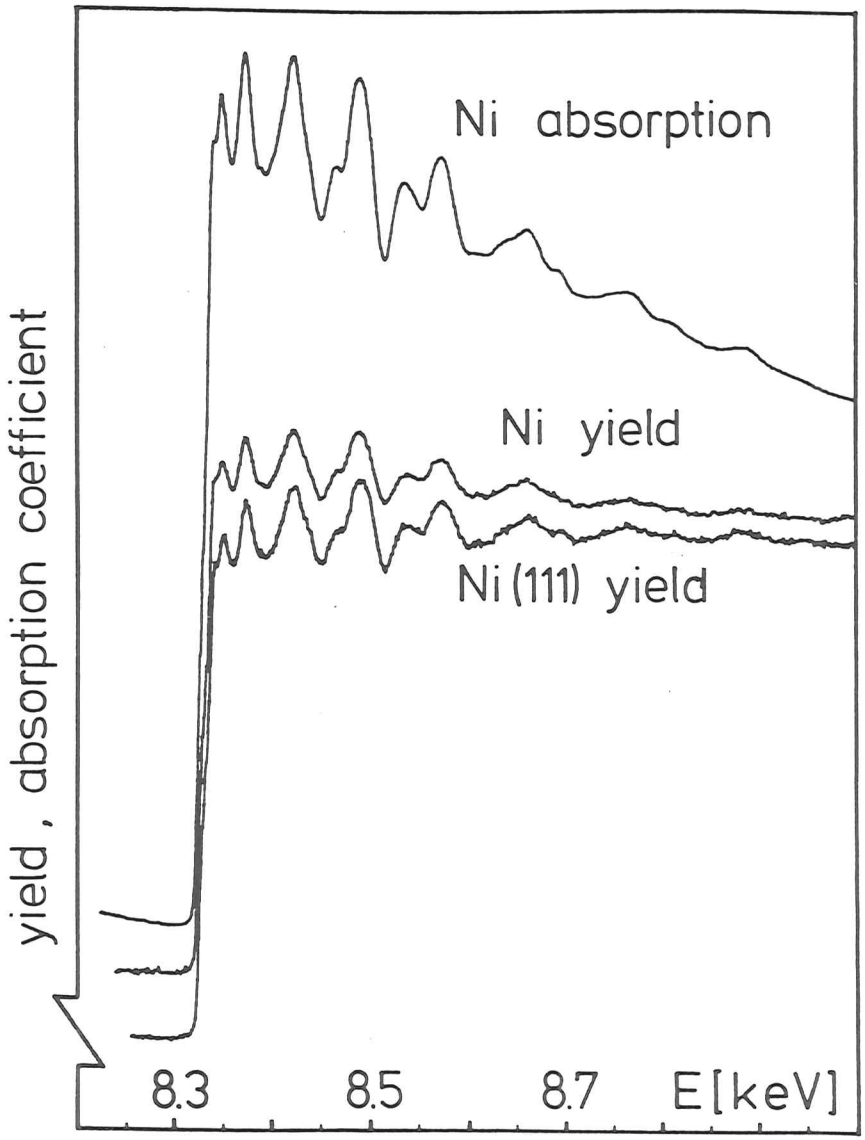
yield, absorption coefficient
Ni absorption
Ni yield
Ni (111) yield
8.3
8.5
8.7
E [keV]

Fig. 22

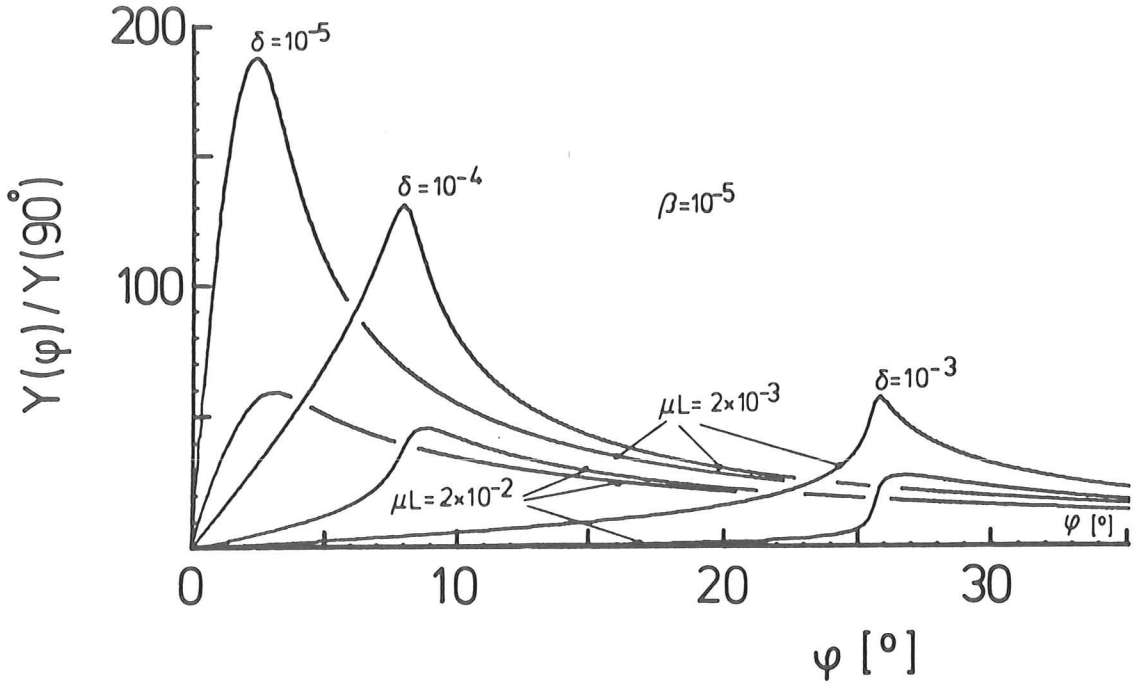
200
100
Y(φ) / Y(90°)
δ = 10⁻⁵
δ = 10⁻⁴
β=10⁻⁵
μL= 2×10⁻³
δ=10⁻³
μL= 2×10⁻²
φ [°]
0
10
20
30
φ [°]

Fig. 23

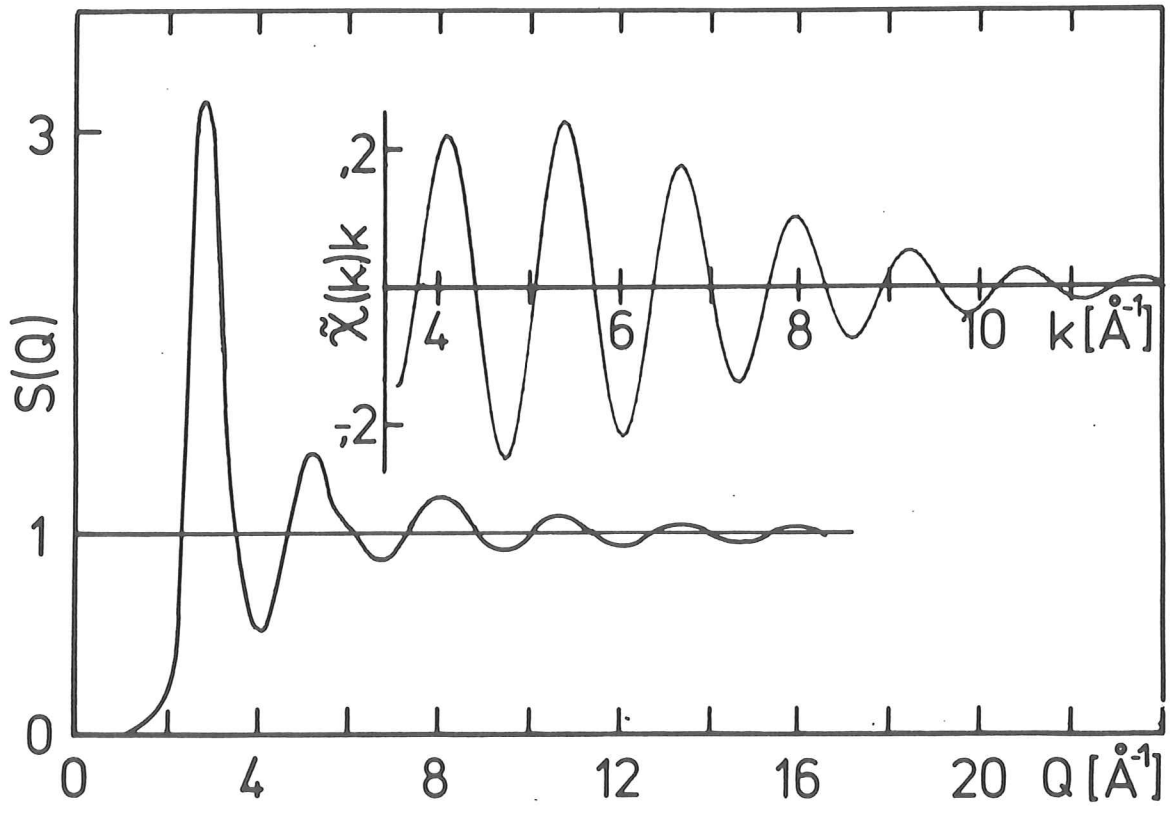
3
1
0
S(Q)
,2
-,2
χ̃(k)k
4
6
8
10
k[Å⁻¹]
0
4
8
12
16
20
Q[Å⁻¹]

Fig. 24

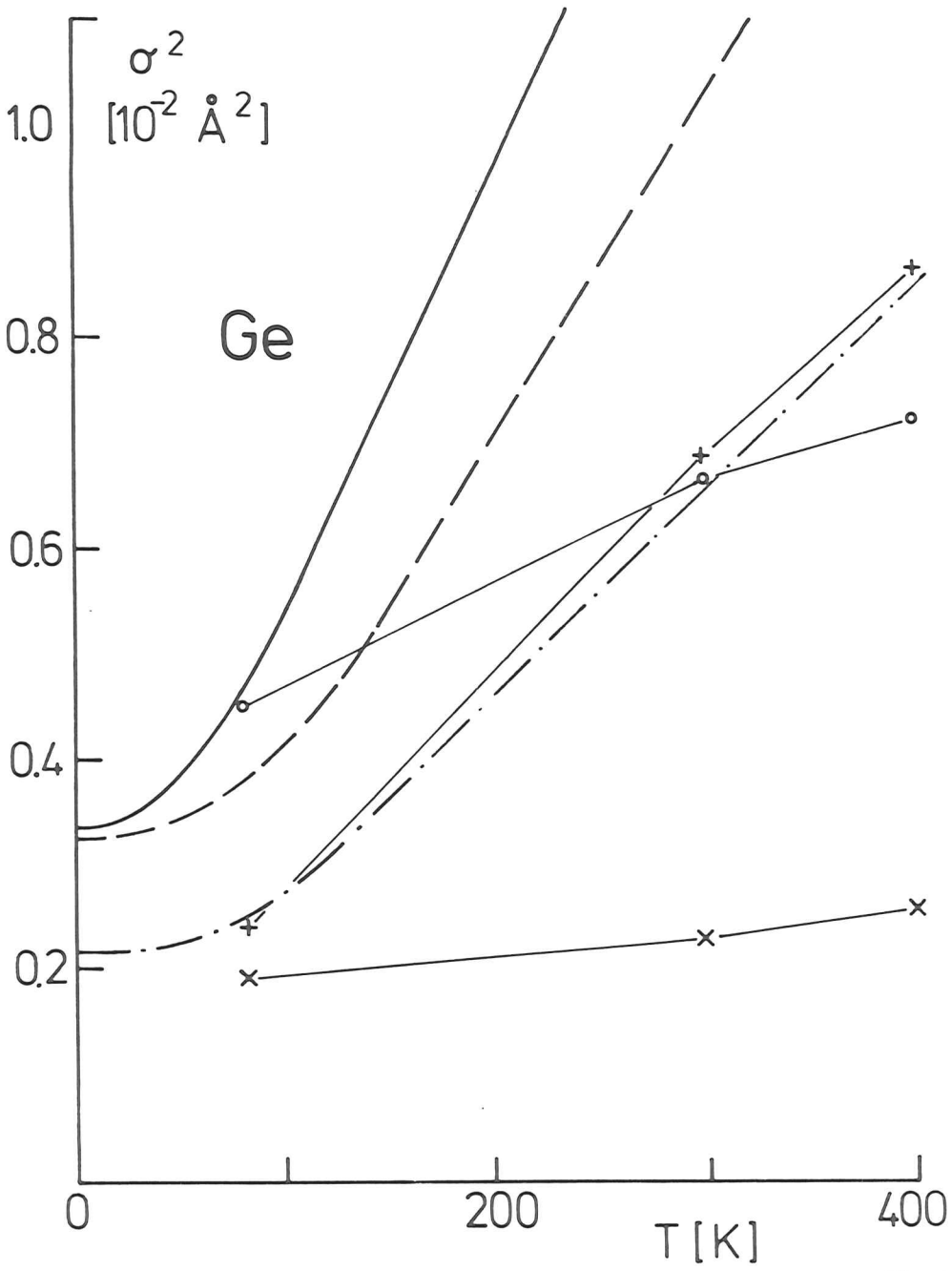
σ²
[10⁻² Å²]
Ge
1.0
0.8
0.6
0.4
0.2
0
200
400
T [K]

Fig. 25

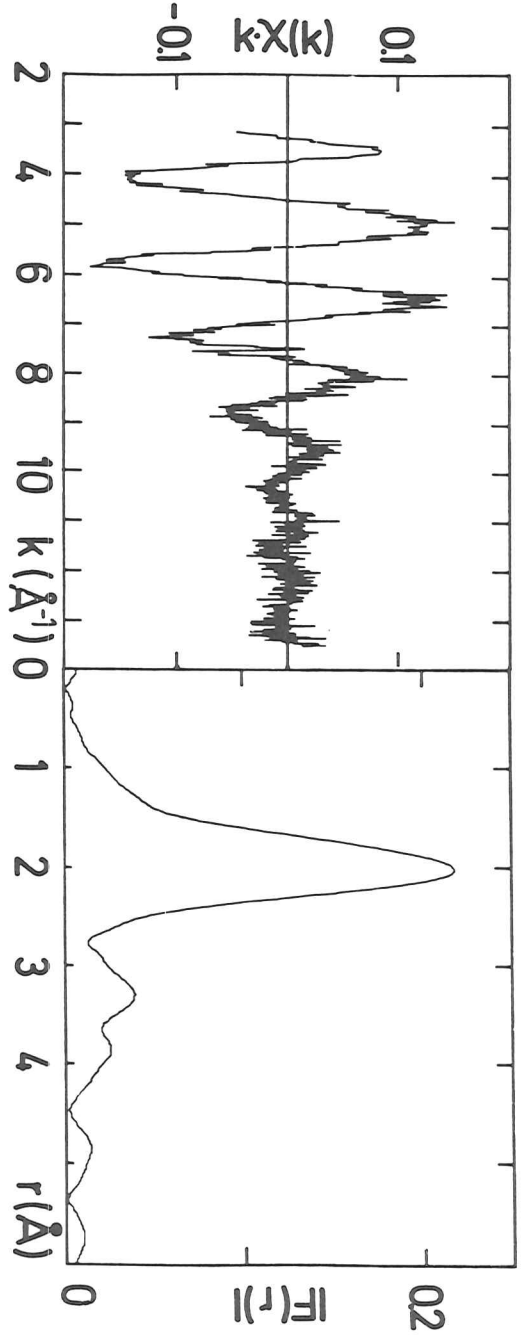
-0.1
k·X(k)
0.1
2
4
6
8
10
k (Å⁻¹)
0
1
2
3
4
r (Å)
0
|F(r)|
0.2

Fig. 26

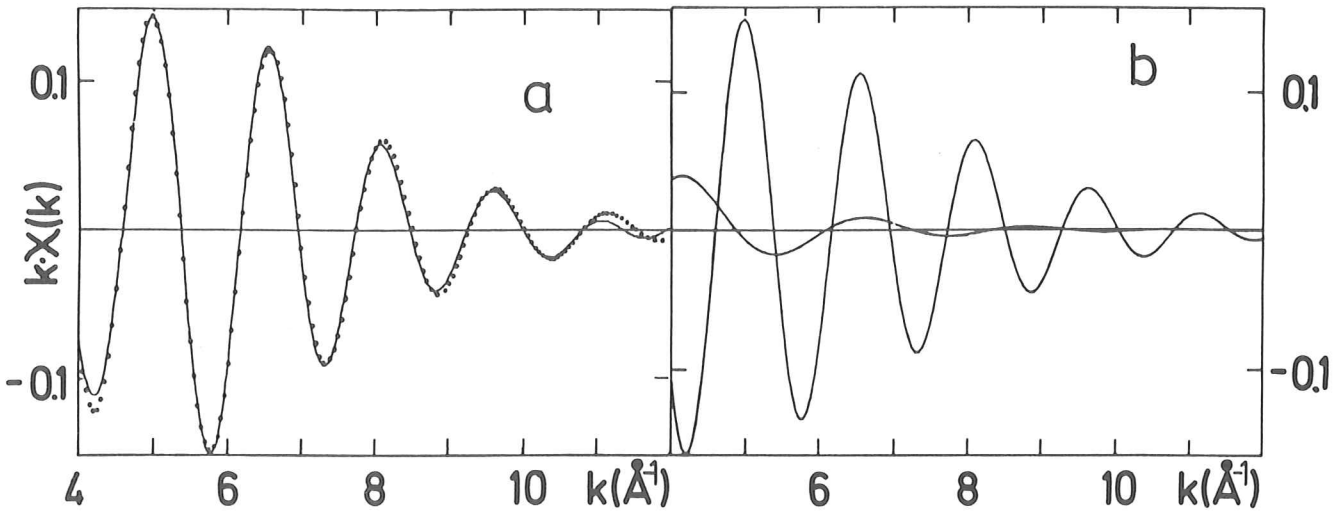
a
b
0.1
-0.1
k·χ(k)
4
6
8
10
k(Å⁻¹)

Fig. 27

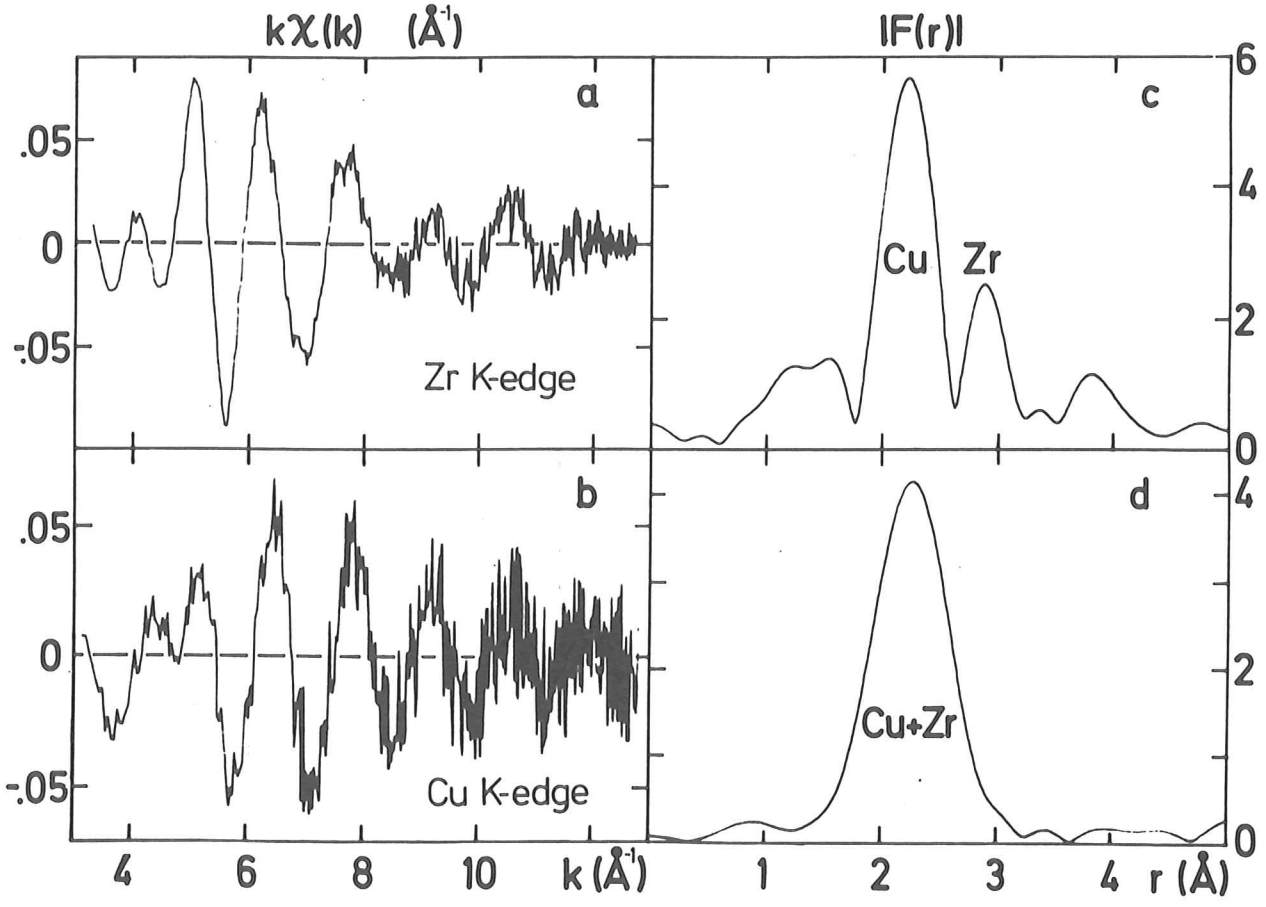
kχ(k) (Å⁻¹)
IF(r)I
a
b
c
d
.05
0
-.05
Zr K-edge
Cu K-edge
Cu
Zr
Cu+Zr
4
6
8
10
k (Å⁻¹)
1
2
3
4 r (Å)

Fig.28

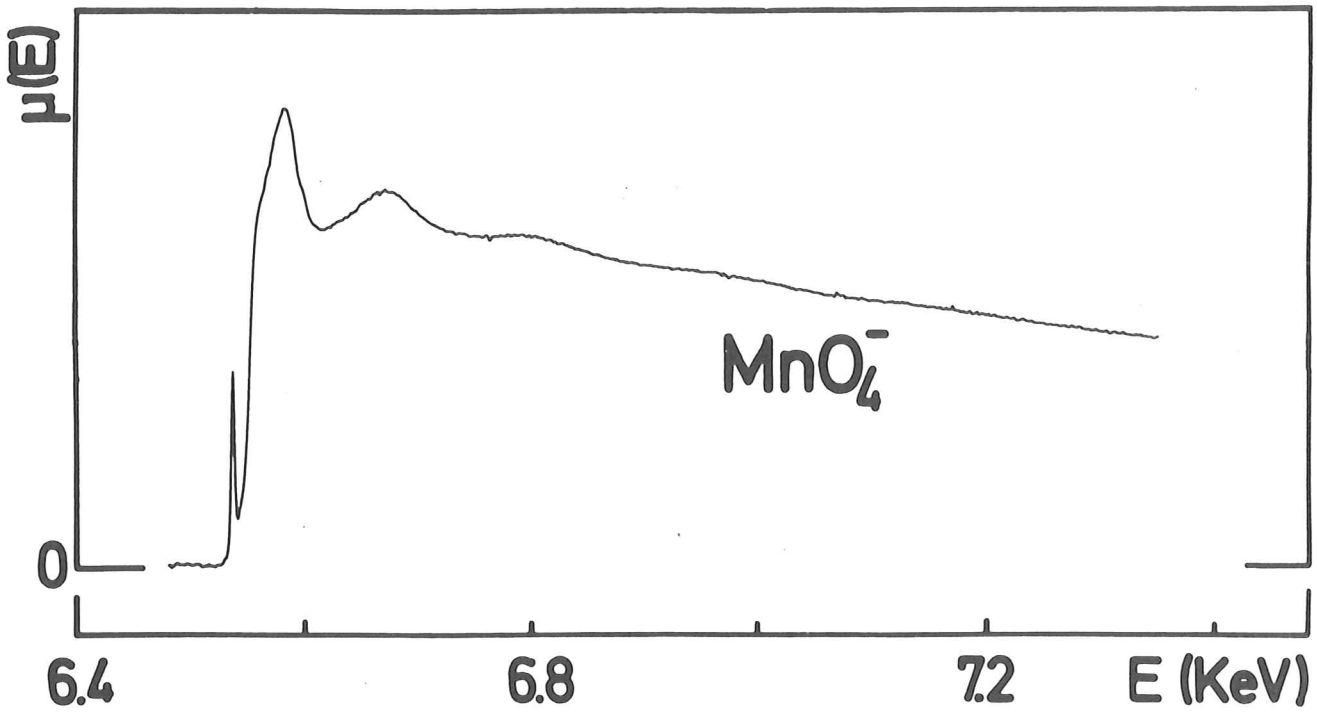

Fig. 29

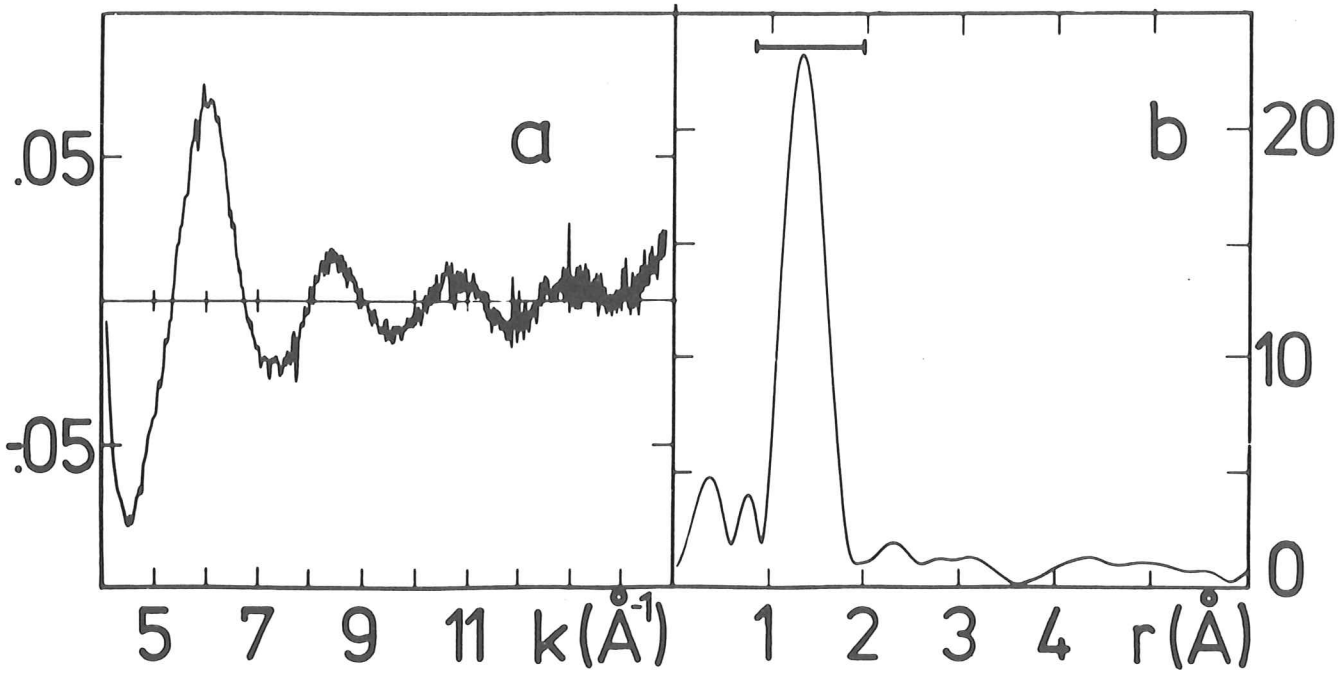

Fig. 30

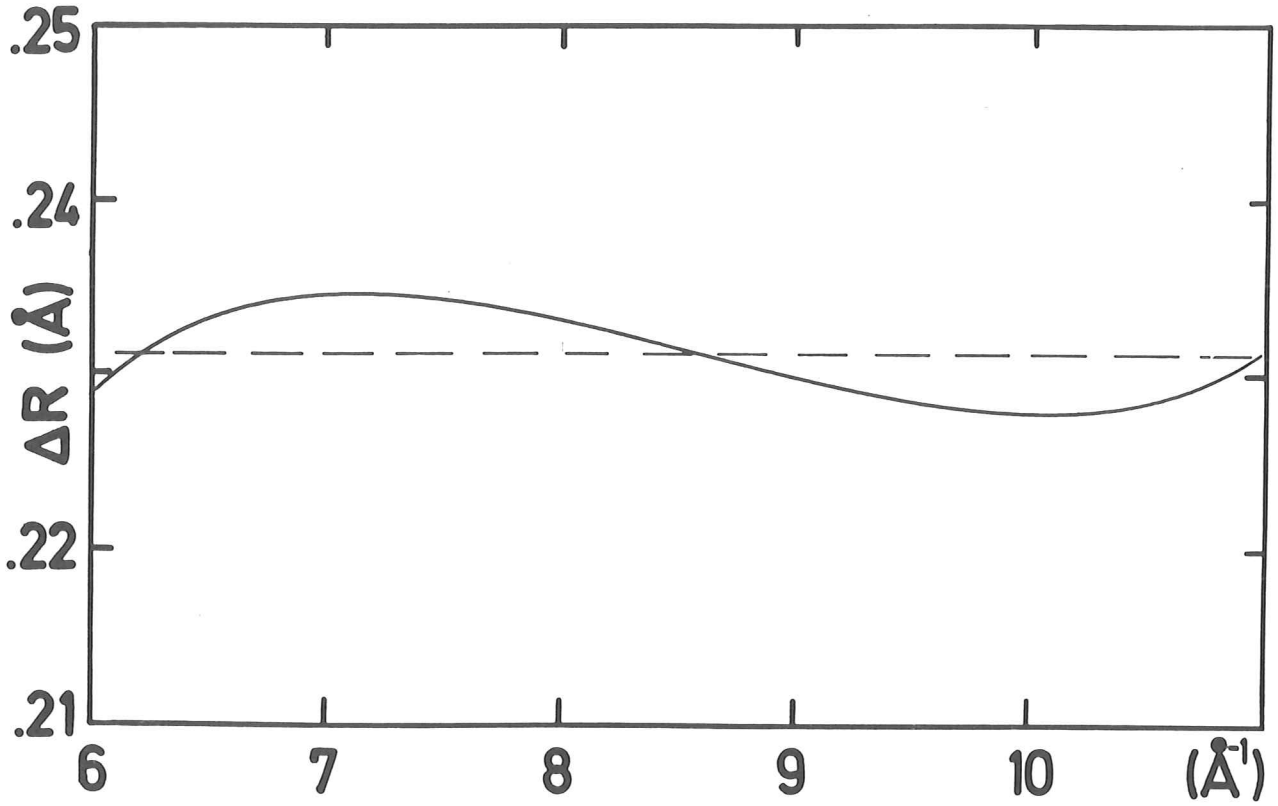

Fig. 31

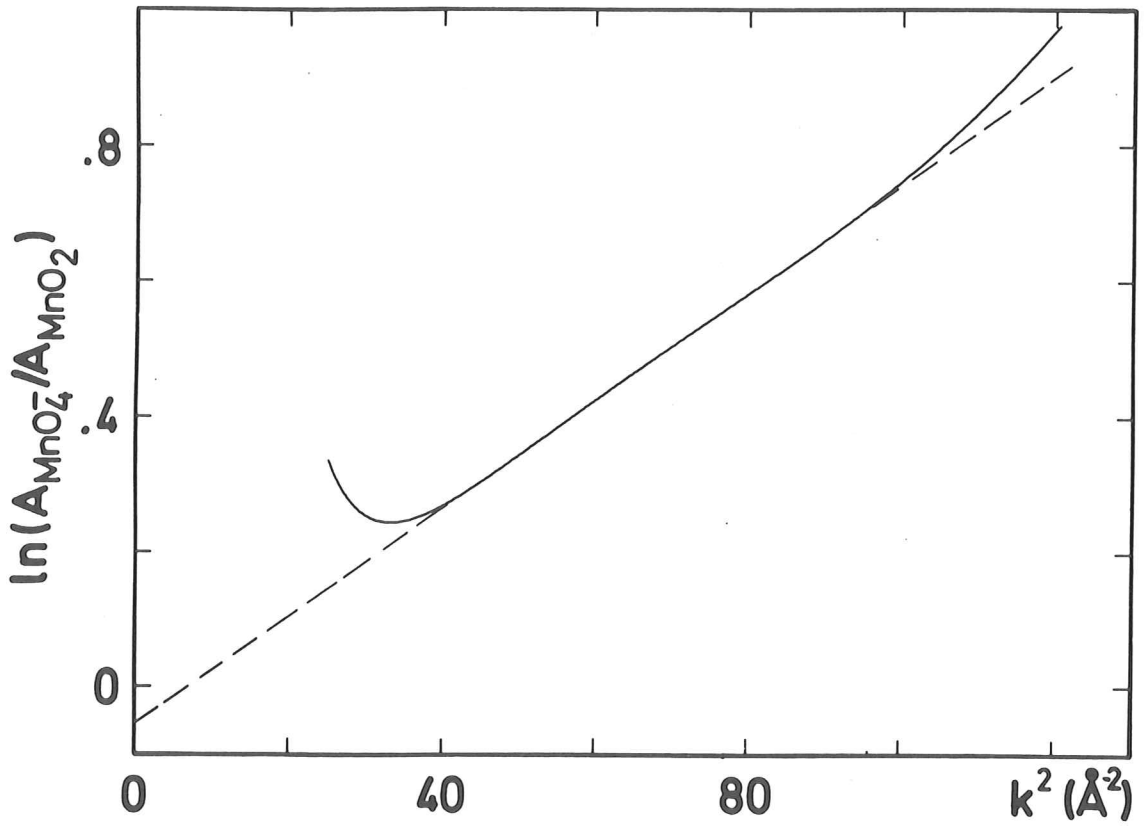

Fig. 32

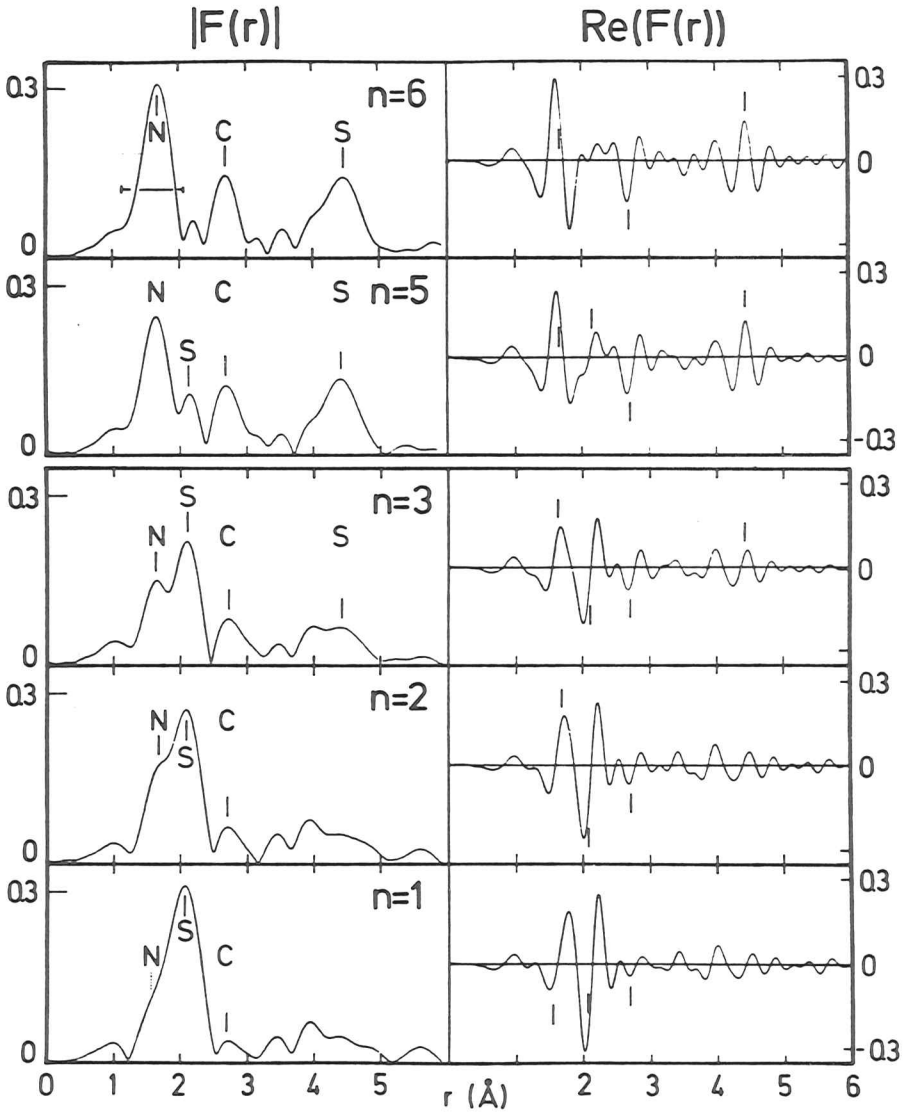
|F(r)|
Re(F(r))
n=6
n=5
n=3
n=2
n=1
N
C
S
0.3
0
-0.3
0 1 2 3 4 5
2 3 4 5 6
r (Å)

Fig. 33

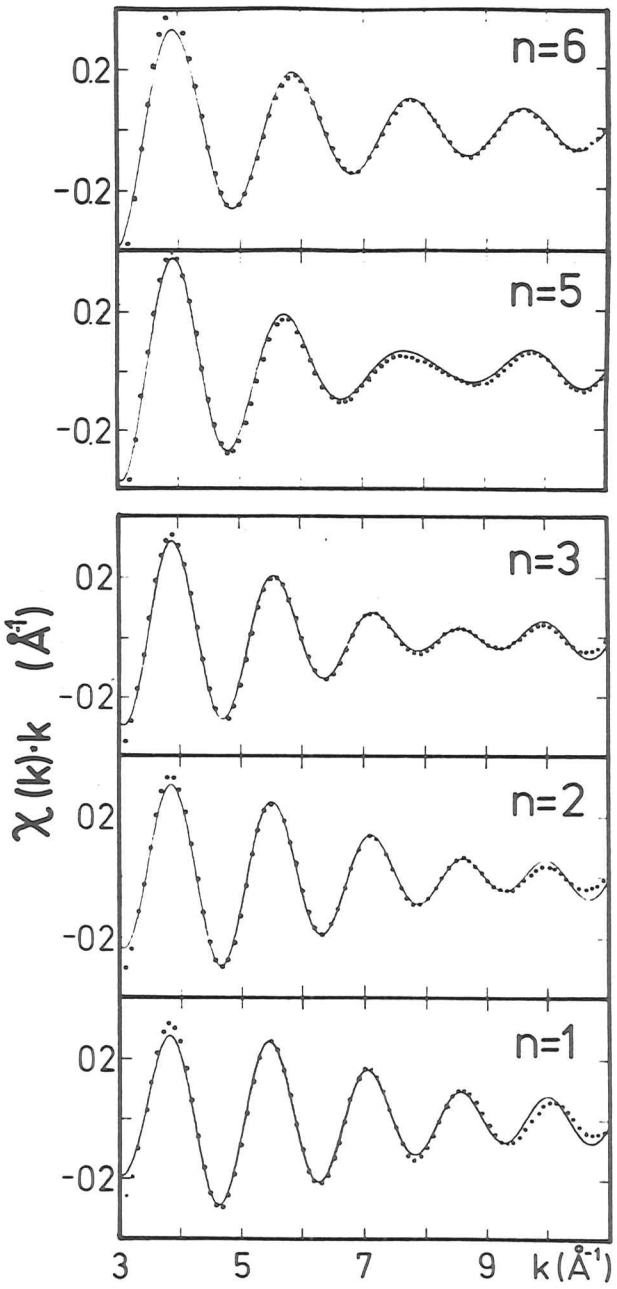
n=6
n=5
n=3
n=2
n=1
0.2
-0.2
χ(k)·k (Å⁻¹)
3 5 7 9 k(Å⁻¹)

Fig. 34

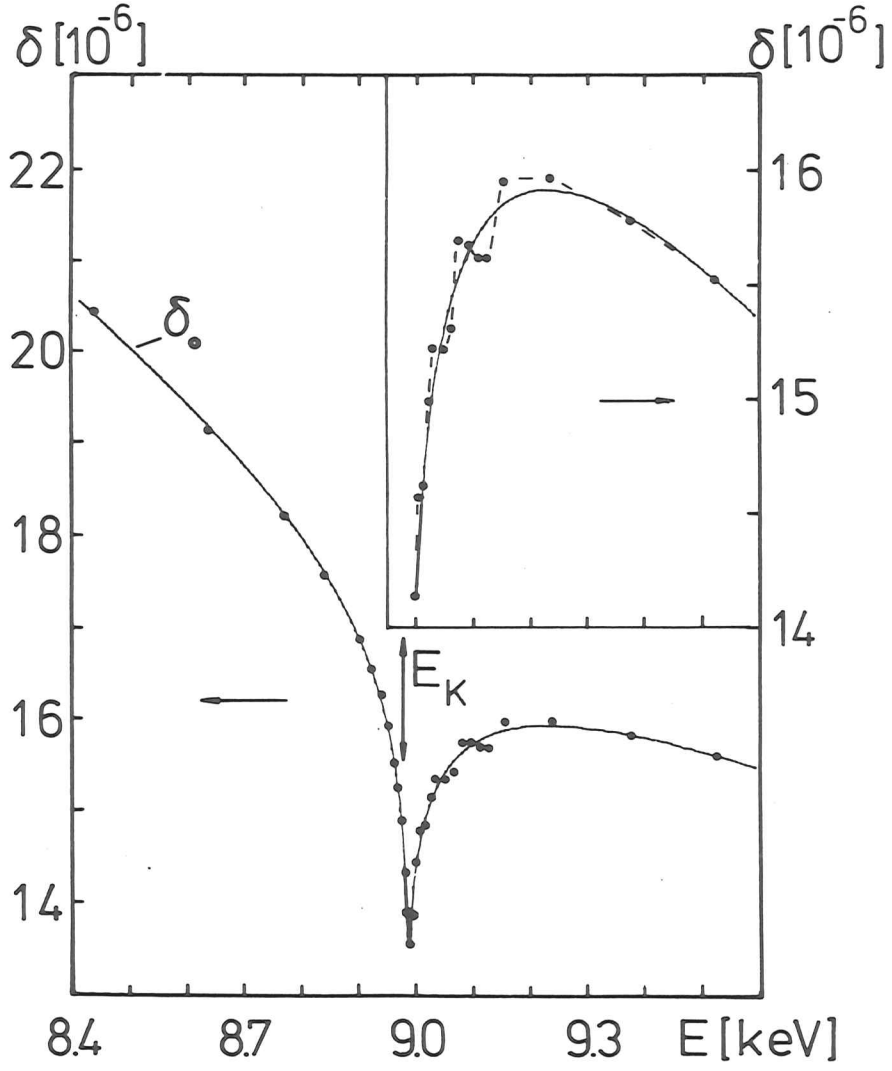
δ [10⁻⁶]
δ [10⁻⁶]
22
20
18
16
14
16
15
14
δ₀
E_K
8.4
8.7
9.0
9.3
E [keV]

Fig 36

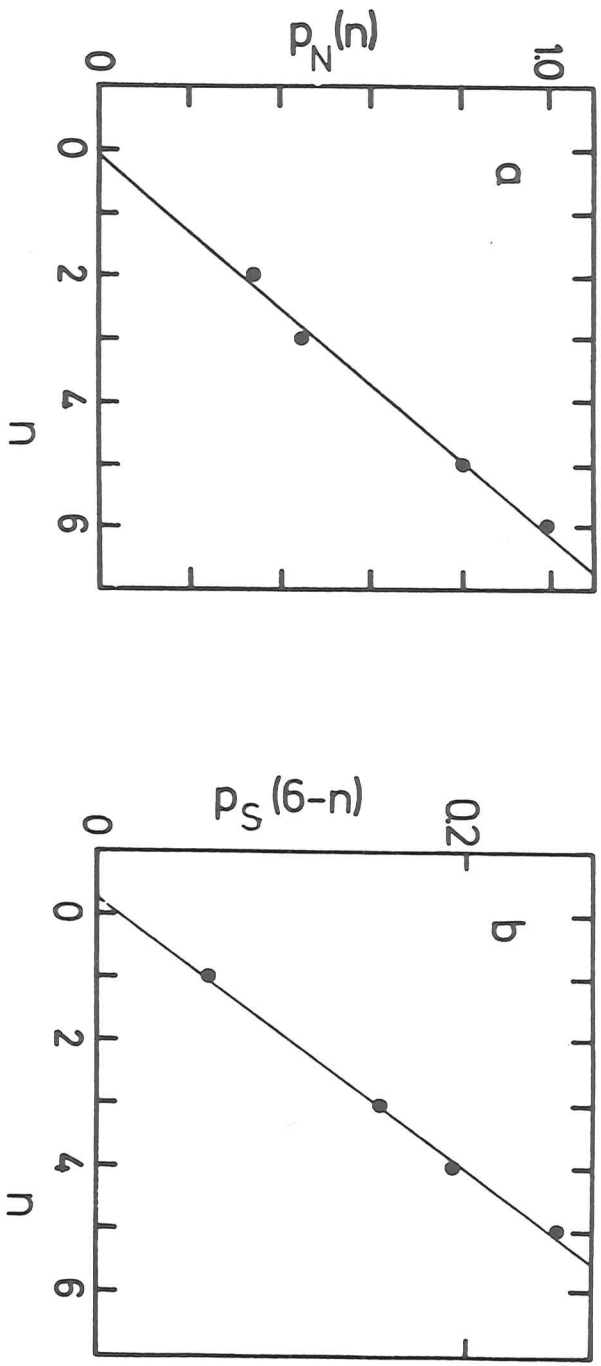
p_N(n)
0
1.0
0
2
4
6
n
a
p_S(6-n)
0
0.2
0
2
4
6
n
b

Fig. 35

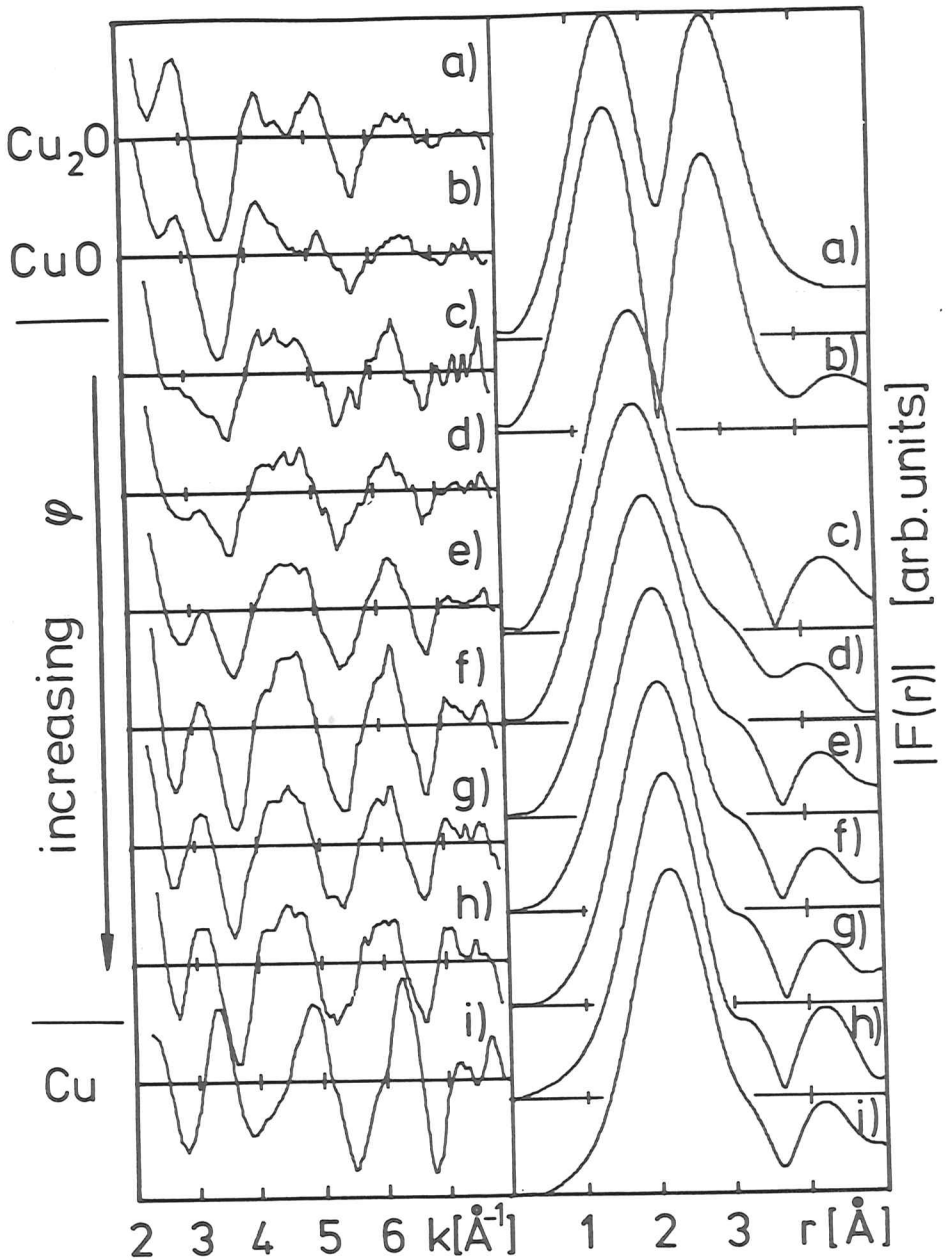
Cu2O
CuO
Cu
increasing φ
a)
b)
c)
d)
e)
f)
g)
h)
i)
2 3 4 5 6 k[Å-1]
1 2 3 r[Å]
|F(r)| [arb.units]

Fig. 37

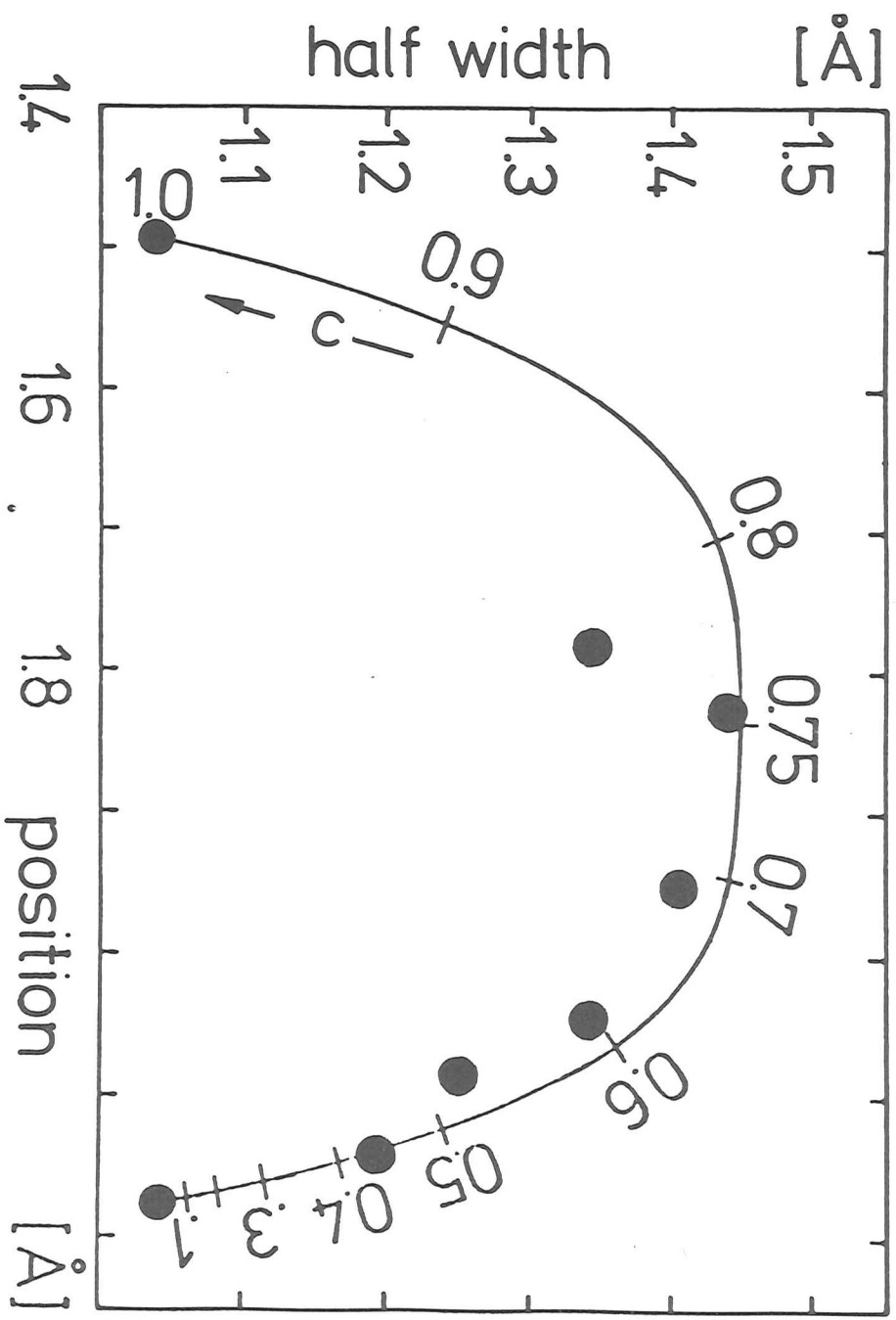
half width [Å]
1.0 1.1 1.2 1.3 1.4 1.5
1.4 1.6 1.8 position [Å]
c
0.9
0.8
0.75
0.7
0.6
0.5
0.4
0.3
0.1

Fig. 38

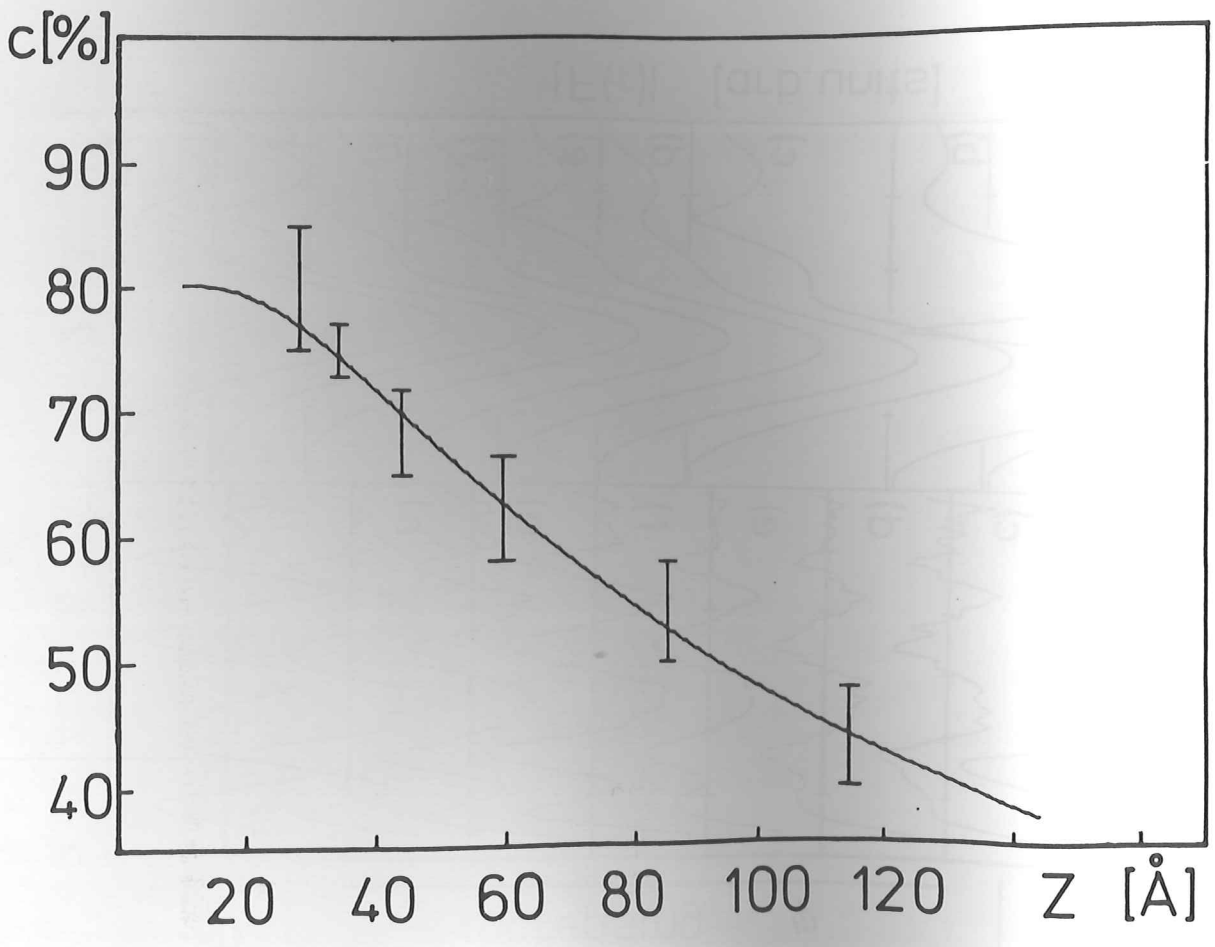

Fig. 39